

Electrospinning Combined with Atomic Layer Deposition to Generate Applied Nanomaterials: A Review

Sesha Vempati,* Kugalur Shanmugam Ranjith, Fuat Topuz, Necmi Biyikli, and Tamer Uyar*



Cite This: <https://dx.doi.org/10.1021/acsnm.0c01120>



Read Online

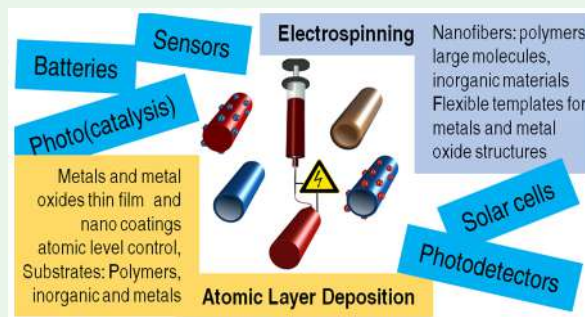
ACCESS |

Metrics & More

Article Recommendations

ABSTRACT: Combining different material processing techniques is one of the keys to obtain materials that depict synergistic properties. In this review, we have reviewed a combination of two highly potential techniques, namely, electrospinning and atomic layer deposition (ALD), in the view of various applications. Over the past 10 years, our research groups are involved in the exploration of employing this combination for a range of applications. We also include some basic information on both the processes and diversity of nanostructures as a result of their combination. Nonwoven nanofiber membranes are excellent candidates for a wide range of applications. Also, they can act as templates to produce various other kinds of nanostructures when combined with ALD in small/large scale production. These nanostructures could be used as such or further subjected to other processing techniques yielding hierarchical structures. In this review, we exclusively survey and highlight the unique capabilities of combined electrospinning and ALD for applications in catalysis, photocatalysis, solar cells, batteries and gas sensors.

KEYWORDS: electrospinning, atomic layer deposition, hierarchical nanostructures, catalysis, batteries, sensors, ALD



INTRODUCTION

Material science crucially includes studies on the properties of various materials and their combinations. Notably, the properties of any material are dependent on the processing methodology. Also, enhancing and tailoring the functionality of an existing material is as important as that of discovering novel counterparts. The intrinsic properties of a material may depend on the physical dimensions, e.g., quantum confinement effect. There is a surge of various material processing techniques asserting some degree of control on the properties and physical dimensions; e.g., pulsed laser deposition,¹ chemical vapor deposition,² hydrothermal growth,^{3,4} electrospinning,⁵ atomic layer deposition (ALD),^{2,6–10} and so on.^{3,11,12} Now, in the context of enhancing and tailoring the functionality of a material, “combination(s)” of various material processing techniques are promising. The combination of electrospinning and ALD could address the needed high-surface area precision-coated functional materials. Indeed, electrospinning is a versatile technique to produce nanofibers from polymers¹³ and nonpolymeric¹⁴ viscoelastic fluids yielding inorganic and ceramic materials. On the other hand, ALD is capable of producing conformal thin films as well as nanostructures (see Table 1).^{15,16} The materials spectra that can be deposited via ALD includes oxides, nitrides, sulfides, and metals among others.^{2,6–10} Individually, these techniques are rather successful to cover a wide range of applications including energy

storage,^{17,18} solar cells,^{19,20} surface passivation,^{20,21} catalysis,^{22–24} and flexible/wearable devices.^{25,26} Also, electrospun nanostructures find potential usage in (photo)catalysis, energy storage,²⁷ solar-cells,^{28,29} filtration,³⁰ the textile industry,³¹ wound dressing,³² drug delivery,³³ and environmental applications.³⁴

The intersecting research areas of ALD and electrospinning capture significant attention due to the versatile applicability (Chart 1). By looking at the fundamental perspective of high surface area to volume ratio, structural integrity, surface electronic structure, and flexibility are some key requirements for high efficiency, either for catalysis,³⁵ solar cells,³⁶ batteries,^{37–44} heterogeneous catalysis,^{4,45,46} antimicrobial activity,⁴⁷ water purification,^{48,49} etc. For example, in the case of solar cells, higher current densities could be obtained for a relatively higher surface area of the device.²⁹ In the case of catalytic reactions^{29,45}/gas sensors,⁵⁰ a higher density of the active sites would be exposed to the reactants. It is found that the sensing performance of the core–shell nanostructures

Received: April 26, 2020

Accepted: May 12, 2020

Published: May 12, 2020

Table 1. Morphological Characterization of Nanostructures Produced with a Combination of Electrospinning and ALD

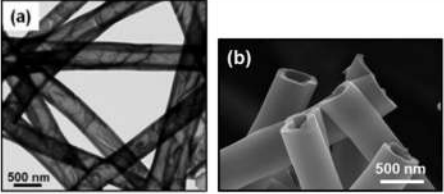
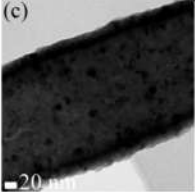
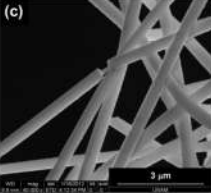
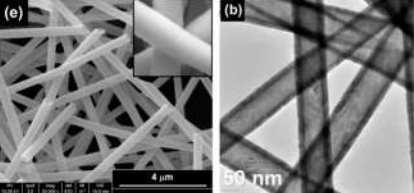
SNo.	Material/ Nanostructure	Precursor	Scanning and/or transmission electron micrographs of the nanostructures
1	TiO ₂ nanotubes of ~75 nm wall thickness synthesized through the thermal decompositio n process	Electrospinning: PVAc, H ₂ O ALD: TIP, H ₂ O, N ₂ -carrier gas	 <p>Micrographs (left) TEM (right) SEM. Reproduced from ref ⁶⁴. Copyright 2011 John Wiley and Sons.</p>
2	ZrO ₂ Core-shell fibers of Poly(ether sulfone)-ZrO ₂ nanofibers	Electrospinning: DMAc, PES ALD: Tetrakis (dimethylamido) zirconium, H ₂ O, N ₂ as a carrier gas	 <p>TEM Micrograph ALD at 250 °C. Reproduced from ref ¹⁰⁷. Copyright 2015 American Chemical Society.</p>
3	HfO ₂ core- shell	Electrospinning: Nylon 6,6, HFIP, formic acid ALD: tetrakis (dimethylamido) hafnium, H ₂ O, N ₂ -carrier gas	 <p>SEM image: 600 cycles HfO₂ deposited at 200 °C on nanofibers of 330 nm average diameter. Reproduced from ref ⁵⁸. Copyright 2013 Elsevier.</p>
4	HfO ₂ hollow nanofibers	Electrospinning: Nylon 6,6; HFIP, formic acid ALD: Tetrakis (dimethylamido) hafnium, H ₂ O, N ₂ carrier gas	 <p>SEM image: HfO₂ hollow nanofibers, deposited at 200 °C with 600 cycles. TEM Image: Micrograph of HfO₂ hollow nanofiber. Reproduced from ref ⁵⁸. Copyright 2013 Elsevier.</p>

Table 1. continued

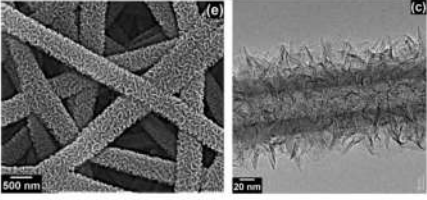
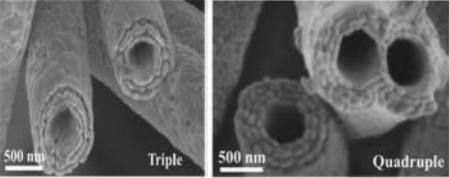
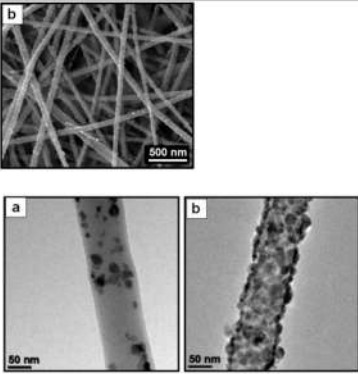
SNo.	Material/ Nanostructure	Precursor	Scanning and/or transmission electron micrographs of the nanostructures
5	AlN/BN bi-shell hollow nanofibers	Electrospinning: nylon 6,6, formic acid ALD: trimethylaluminum, N ₂ /H ₂ plasma, Ar-carrier gas	 <p>(left) SEM (right) Bright field TEM image hollow nanofiber having an average inner fiber diameter of ~100 nm with an average wall thickness of ~20 nm and ~35 nm of AlN and BN, respectively. Reproduced from ref⁵⁵. Licensed under a Creative Commons Attribution (CC BY) license, American Institute of Physics.</p>
6	ZnO/ZnAl ₂ O ₄ multilayered nanotubes: Multilayered deposition with varying the number of cycles, 60 °C. Nanotubes are obtained after calcining at 450 °C.	Electrospinning: PAN, DMF ALD: DEZn, TMA.	 <p>SEM image: ZnO/ZnAl₂O₄ triple and quadruple co-centric nanotubes annealed in air at 900 °C. Reproduced from ref¹⁰⁸. Copyright 2016 Royal Society of Chemistry.</p>
7	ZnO nanoparticles (NPs)	Electrospinning: Nylon 6,6, formic acid ALD: DEZn, H ₂ O, N ₂ - carrier gas	 <p>SEM images (left) nylon-ZnO NPs, (middle) TEM images nylon-ZnO NPs, (right) nylon-ZnO NPs (highly dense). Reproduced from ref¹⁰⁹. Copyright 2013 Royal Society of Chemistry.</p>

Table 1. continued

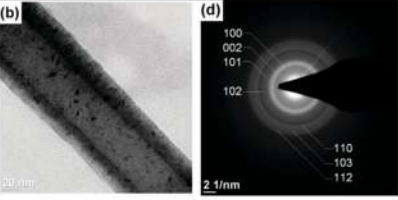
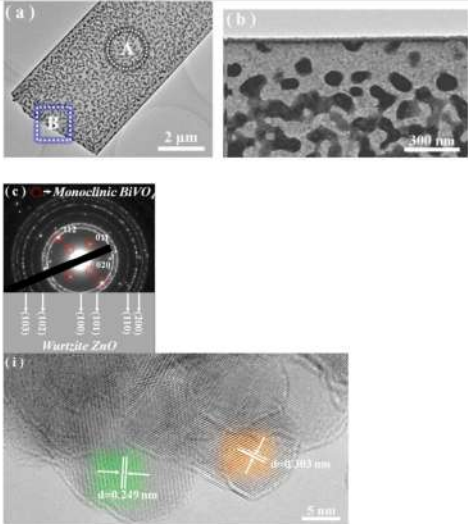
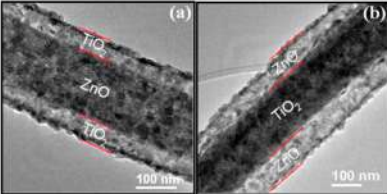
SNo.	Material/ Nanostructure	Precursor	Scanning and/or transmission electron micrographs of the nanostructures
8	Nylon-GaN core-shell nanofiber produced through hollow cathode plasma assisted ALD at 200 °C.	Electrospinning: Nylon 6,6, formic acid ALD: TMG, 5N- grade N ₂ , H ₂ , Ar	 <p>(left)TEM image and (right) SAED pattern Reproduced from ref⁵⁴. Copyright 2015 Royal Society of Chemistry.</p>
9	BiVO ₄ -ZnO microbelts	Electrospinning: PVP, Bi(NO ₃) ₃ ·5H ₂ O and VO(acac) ₂ , diisopropylamine ALD: DEZn, H ₂ O, N ₂ -carrier gas	 <p>TEM images: (top row) BiVO₄@ZnO microbelts for 400 cycles of deposition. (bottom row) The corresponding SAED pattern recorded from the single microbelt recorded from marked area A in the top row and a HRTEM image recorded from the marked area B in the top row. Reproduced from ref¹¹⁰. Copyright 2018 Elsevier.</p>
10	ZnO/TiO ₂ and TiO ₂ /ZnO core-shell nanofibers	Electrospinning: PVP, TIP, ZnAc DMF, EtOH, glacial acetic acid. ALD: TDMAT, DEZn, and HPLC grade H ₂ O	 <p>TEM images: Core-shell heterojunction nanofibers (left) ZnO-TiO₂, (right) TiO₂-ZnO. Reproduced from ref⁴⁶. Copyright 2014 Royal Society of Chemistry.</p>

Table 1. continued

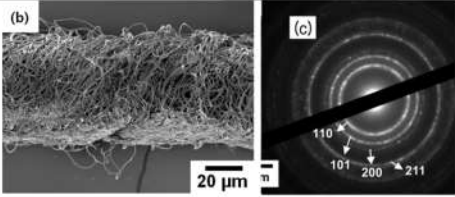
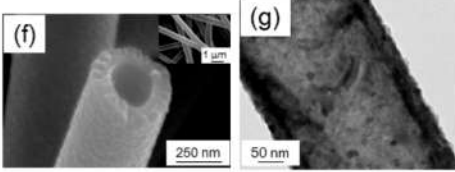
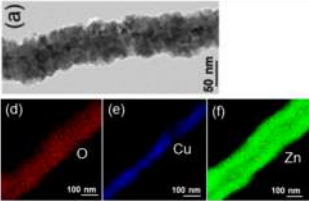
SNo.	Material/ Nanostructure	Precursor	Scanning and/or transmission electron micrographs of the nanostructures
11	SnO ₂ microtube yarns obtained by twisting the sacrificial PAN nanofibers and deposit SnO ₂	Electrospinning: PAN, DMF ALD: Dibutyltin-diace- tate	 <p>SEM images: (left) SnO₂ coated yarn by ALD and (right) SnO₂ nanotube yarn after calcination. Reproduced from ref ¹¹¹. Copyright 2011 IOP Publishing.</p>
12	TiO ₂ /ZnO double layered hollow nanofibers ALD of two different inorganic materials	Electrospinning: PVAc, EtOH ALD: TIP, DEZn, H ₂ O	 <p>SEM image: (left) TiO₂/ZnO double layer hollow for 350 cycles. TEM image: (right) TiO₂/ZnO double layer hollow fiber with 8 nm thick ZnO outer layer. Reproduced from ref ⁵⁷. Copyright 2014 American Chemical Society.</p>
13	CuO ZnO core-shell structure	Electrospinning: PVA, copper acetate, H ₂ O ALD: DEZn, H ₂ O, N ₂ -carrier gas	 <p>TEM image: (left) Low-magnification TEM image of an individual p-CuO/n-ZnO core-shell nanofiber with a 16-nm-thick shell layer. What follows are EDS elemental maps are shown for O, Cu and Zn. Reproduced from ref ¹¹². Copyright 2014 IOP Publishing.</p>

Table 1. continued

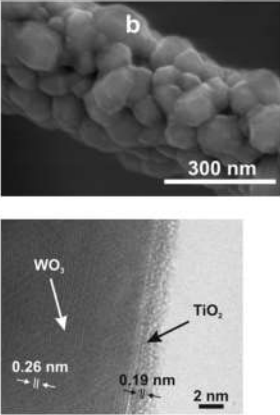
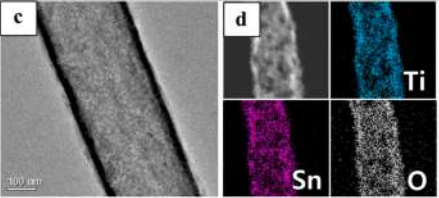
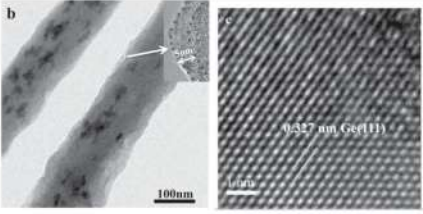
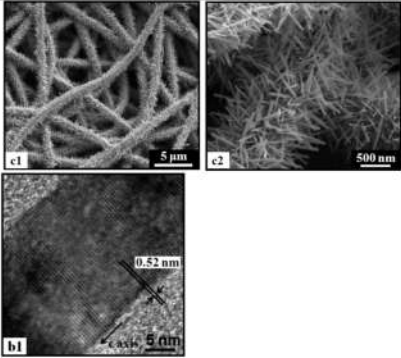
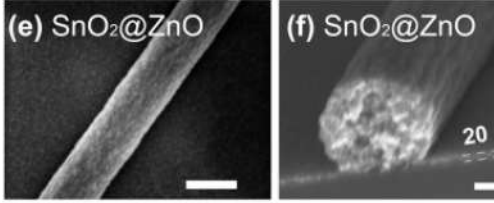
SNo.	Material/ Nanostructure	Precursor	Scanning and/or transmission electron micrographs of the nanostructures
14	Core-shell WO ₃ /TiO ₂ Treated at 550 °C to yield WO ₃ nanofibers.	Electrospinning: ammonium metatungstate, PVP. ALD: TiCl ₄ , H ₂ O, N ₂ -carrier gas	 <p>SEM images: (left) WO₃/1.5 nm TiO₂ TEM Image: (right) HRTEM image of the WO₃/1.5 nm TiO₂. Reproduced from ref¹¹³. Copyright 2013 John Wiley and Sons.</p>
15	TiO ₂ -SnO ₂ - TiO ₂ trilayered tubular nanostructures	Electrospinning: PAN, DMF ALD: Dibutyltin diacetate, TIP	 <p>TEM image: (left) shows the trilayered tubular structure, (right) shows EDS mapping of a selected region shown Ti, Sn and O. Reproduced from ref¹¹⁴. Copyright 2017 Springer.</p>
16	Germanium@ graphene@Ti O ₂ core-shell	Electrospinning: PVP, graphene in 2.2 g of DMF, GeCl ₄ . ALD: TIP, H ₂ O, N ₂ -carrier gas	 <p>TEM images: (left) Ge@G@TiO₂ (right) HRTEM of Ge showing nanocrystalline Ge grains in a highly ordered matrix. Reproduced from ref³⁹. Copyright 2016 John Wiley and Sons.</p>

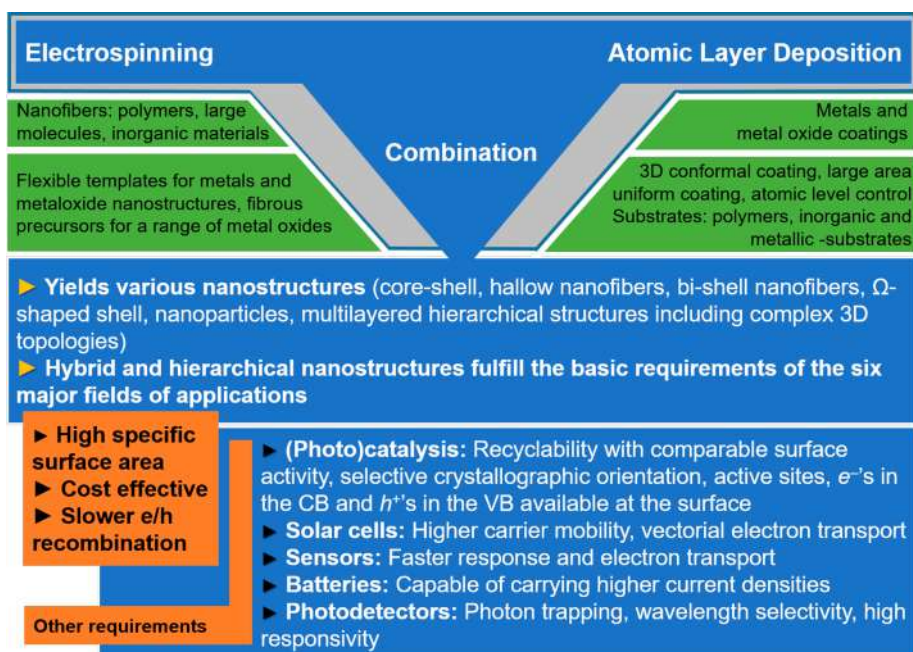
Table 1. continued

SNo.	Material/ Nanostructure	Precursor	Scanning and/or transmission electron micrographs of the nanostructures
17	ZnO nano needles core- shell structure	Electrospinning: PAN, DMF, ALD: DEZn, H ₂ O, N ₂ -carrier gas	 <p>SEM images: (left and middle) Poly(acrylonitrile)/ZnO needle nanofibers at different magnifications. TEM image: (right) HRTEM image of ZnO needle. Reproduced from ref⁴. Copyright 2014 Elsevier.</p>
18	Ω shaped ZnO coated SnO ₂ nanofibers	Electrospinning: SnCl ₂ ·2H ₂ O, EtOH, PVP, DMF ALD: DEZn, H ₂ O, N ₂ -carrier gas	 <p>SEM image: (left) Side view of SnO₂ nanofiber and (right) SnO₂@ZnO showing the Ω shape. Scale bars are 200 nm in (left), and 100 nm in (right). Reproduced from ref⁵³. Copyright 2017 John Wiley and Sons.</p>

65 results from the radial modulation of the electron depletion
66 region as a function of the thickness of the shell.⁵¹
67 Furthermore, due to the band alignment, the hybrid semi-
68 conducting structures, in general, possess an internal electric
69 field. They also depict the tunability of electronic and optical
70 properties.⁵² This built-in electric field could separate the
71 photogenerated charge carriers before recombination, which
72 has significant potential in solar cells, photodetectors, and
73 photocatalysis.⁴⁶ These heterostructures facilitate trapping of
74 photons and wavelength selectivity could also be achieved
75 when the photons are suitably confined.⁵³ The combination
76 produces core-shell,⁵⁴ bishell hollow,^{55–57} hollow nano-
77 fibers,^{45,58–62} and metal nanoparticle-loaded^{47,63–65} nano-
78 fibrous templates (see Chart 1). This combination can be
79 extended to form advanced multilevel structures, such as
80 Al₂O₃/Ni/Al₂O₃,⁶⁶ SrTiO₃/SrTiO₃,⁶⁷ polymer/TiO₂/Pt-
81 nanoparticles,⁶⁸ etc. Furthermore, inorganic material coated
82 polymer fibers could be subjected to hydrothermal,⁴ chemical
83 bath,⁶⁹ and microwave-assisted solvothermal⁷⁰-like methods.
84 For instance, hydrothermal growth⁴ yields nanorods of high
85 crystalline quality, which provides highly efficient channels for
86 the transport of both electrons and holes to the surface, while
87 the solvothermal technique⁷⁰ can produce metal-organic
88 frameworks.

As discussed earlier, the application potential of these
techniques is reflected in a significant number of publications
and patents on catalysis, batteries, and sensor applications
(Figure 1). Keeping this in mind, this review covers the
literature strictly focusing on the combination of electro-
spinning and ALD. Figure 1a shows the year-wise number of
publications, while Figure 1b shows three major corresponding
research topics. By given the industrial applicability of these
topics, we have also plotted the year-wise number of patents in
Figure 1c. We start the review by briefly discussing the
processes of electrospinning and ALD.

Electrospinning. A charged polymer jet is accelerated
(within an electric field of 10⁵–10⁶ V/m) toward the counter
electrode from a fine nozzle forming a Taylor cone.¹³ The
electrostatic repulsion between surface charges induces
“splaying” of the cone into several fine strands and
continuously drawn nanofibers onto the substrate (counter
electrode). The substrate can be, for example a rotating drum,
which yields aligned nanofibers when the spinning and
collection rates are balanced.⁷¹ A cartoon of the electro-
spinning process and various types of collecting electrodes are
shown in Figure 2. The schematic also shows core-shell,
triaxial, and multineedle spinnerets. Such spinnerets, together
with the formulation parameters, enable the production of

Chart 1. Salient Features of Electrospinning, Atomic Layer Deposition and Their Combination Are Shown^a

^aIt also shows a broad range of hierarchical nanostructures as a result of this combination. The chart also highlights the applicability of these nanostructures that covers the basic requirements of each of the major field of application.

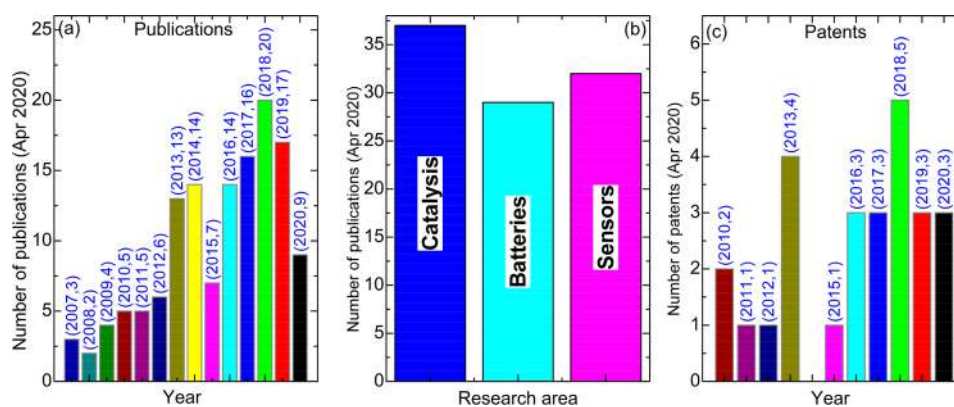


Figure 1. Year-wise statistical analyses on the research topic “electrospinning + atomic layer deposition” (a) number of publications, (b) major research areas, and (c) number of patents. Data updated as of April 24, 2020.

113 fibers with different morphologies, such as hollow, flat/ribbon,
 114 core-shell, porous, and Janus. The electrospinning process has
 115 been applied to produce microns to sub-100 nm sized fibers
 116 from a rich variety of materials, like polymers, ceramics,
 117 nonpolymeric materials,⁷² nanocomposites,⁷³ etc. up to the
 118 industrial-scale.^{74–77} Electrospinning also finds vast applic-
 119 ability in tissue engineering,⁷⁸ water-treatment,⁷⁹ and the food
 120 packing industry.⁸⁰ It has also been adapted to produce a
 121 number of other nanostructures, such as microchannels and
 122 tubes,⁸¹ porous,⁸² hollow, or core-shell structures (e.g.,
 123 biphasic nanofibers with a conducting core with an insulating
 124 shell⁸³). It is also possible that the polymers that are
 125 intrinsically microporous can be subjected to electrospinning
 126 to obtain a relatively higher surface area to volume ratio when
 127 compared to that of the nonporous counterparts.⁸² The
 128 polymer of intrinsic microporosity has a high fractional free-
 129 volume (26%) and is reported to have a BET surface area of
 130 760 m²/g.⁸⁴

Up-Scaling of Electrospinning. Apart from optimization 131
 of the basic electrospinning parameters, up-scaling of the 132
 process usually employs multispinnerets and a suitable power 133
 supply. Also certain changes to the collecting electrodes need 134
 to be implemented depending on the application. Since the 135
 nanofibers are subjected to ALD, it is important to collect the 136
 nanofibers such that the additional precursor diffusion step is 137
 feasible. In fact, various companies supply the laboratory and 138
 industrial-scale components for electrospinning for different 139
 applications. They include Spingenix, Inovenso, Bioinicia, 140
 Elmarco, Yflow, IME, RevolutionFibres, Nanofiber Solutions, 141
 Spraybase, Mecc Co., Ltd., and so on. Electrospinning has been 142
 successfully exploited in industry. The industrial aspect of 143
 electrospun nanofibers is directly visible, where a number of 144
 companies around the globe (Europe,^{85–93} USA,^{94–96} 145
 Asia,^{97,98} Japan,⁹⁹ South Africa,¹⁰⁰ New Zealand,¹⁰¹) produce 146
 nanofibers for various applications. Some of these companies 147
 not only design but also manufacture electrospun nanofibrous 148
 materials for filter media, biomedical applications, wound 149

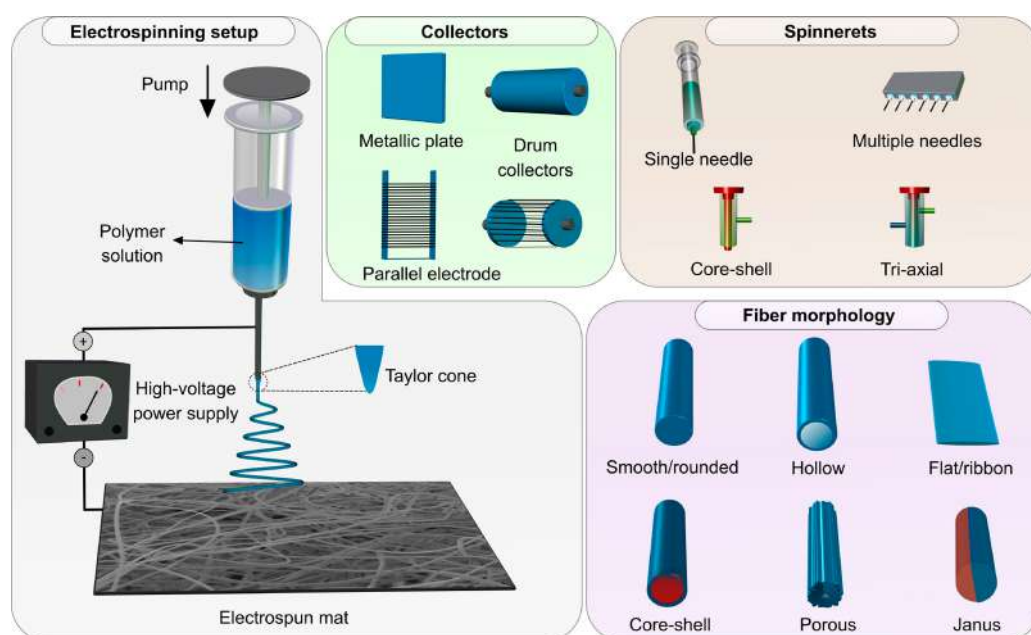


Figure 2. Schematic of the electrospinning process. Schematic also shows typical collectors and spinnerets. Reproduced from ref 80. Copyright 2020 Elsevier.

150 dressing, drug delivery systems, textiles, cosmetics and hygiene
 151 products, etc. Readers are advised to refer to a review by
 152 Persano et al.⁷⁴ and other references^{74–77} for further details on
 153 the industrial up-scaling of electrospinning. For large scale
 154 production of electrospun nanofibers, multinozzle¹⁰² or
 155 nozzleless^{92,100} electrospinning could be employed. The
 156 electrospinning yield can be enhanced using alternative
 157 current, which relies on an electrostatic field with periodically
 158 changing polarity. Alternative current electrospinning yields
 159 multiple times higher productivities achieved with direct
 160 current electrospinning.¹⁰³

161 **Advantages.** The major significant advantages of the electrospinning process can be listed as the following. (1) This technique is relatively simple, (2) cost-effective (a few thousand dollars) to implement, (3) nanofibers of high surface area to volume ratio from a wide variety of polymers and precursors of ceramic, inorganic, and metals, (4) any modification/functionalization is relatively easy, (5) it allows one to produce nanofibers of composites, (6) nanofibers can be collected onto many different surfaces such as glass, metals, water, etc., (7) various nanofibrous structures can be synthesized using hierarchical methods, (8) polymer chain ordering or macromolecular crystallinity increases, and (9) feasibility of industrial level high-volume mass-production.

174 **Disadvantages.** There some disadvantages of the electrospinning process. (1) This technique requires viscoelectric precursor, (2) conductivity should be at a moderate level for easy electrospinning, (3) obtaining single crystalline and continuous inorganic fibers are rather difficult, (4) needs the usage of solvents which may be toxic, (5) insufficient cell infiltration and inhomogeneous cell distribution in tissue engineering applications, (6) no/very-limited control on 3D porosity, (7) diameter of the nanofiber cannot be controlled with high precision, (8) bead formation may be inevitable as the diameter of the fiber decreases, where beads reduce the surface area to volume ratio.

186 **Hardware and Cost of Ownership.** Electrospinning is
 187 one of the very economical techniques to produce nanofibers.

As shown in Figure 2, the setup requires a syringe pump, collection screen, and a high voltage power-supply. Depending on the number of spinning needles (Figure 2), an appropriate power supply needs to be employed so that sufficient current is supplied. Additionally, the whole setup can be installed in an enclosure. This enables continuous spinning where the influence of propellant air is reduced. A lab-scale, commercial setup costs some 1000 USD including a user control on the various features, such as speed of rotating mandrel, duration of the spinning, flow rate in the syringe pump, heating the spinning environment up to 45 °C, and so on. To produce inorganic nanofibers, an oven is required which costs around 1500 USD. Similar to other fiber production techniques, the precursor polymeric materials and relevant solvents are not very expensive. The applicability of this technique to various polymers is one of the most important aspects. When the polymeric nanofibers are used as templates, then a relatively wide distribution of molecular weight of the polymer would still work, reducing the total cost. However, additional cost incurs from the precursor for inorganic nanofibers. Perhaps, during industrial scale production, the evaporated solvent could be recovered through condensing the vapors. This not only makes the whole process cost-effective but also environmentally friendly.

Atomic Layer Deposition. ALD is a low-temperature chemical vapor deposition technique where the material growth is governed by sequential self-saturating gas–solid surface reactions.^{7–10} Conventional gas-phase reactions and thermal decomposition of precursor molecules are eliminated by temporally or spatially separated half-cycles, which leads to digital/pulsed film deposition that proceeds with self-limiting ligand-exchange surface reactions only.^{8,9}

The typical unit deposition cycle of a conventional ABAB-type ALD process consists of four steps: (i) dosing of the metal-containing precursor, which reacts with the active surface groups via chemisorption until surface saturation is achieved, (ii) purging step with an inert gas flow, which will completely remove the excess precursor molecules as well as

226 the ligand-exchange reaction byproducts, (iii) dosing of the
227 second precursor, which is in general defined as the coreactant,
228 which likewise reacts with the chemisorbed surface groups *via*
229 ligand exchange reactions until saturation, (iv) second purging
230 cycle to evacuate the reactor chamber from excess amounts of
231 precursors and reaction byproducts.

232 As precursor molecules do not react with themselves and
233 both precursors react only with the chemisorbed groups on the
234 substrate surface, gas-phase chemical vapor deposition-type
235 reactions are entirely eliminated. Each unit cycle results in a
236 material deposition of a certain film thickness, which is mostly
237 a fraction of a monolayer, and is defined as the growth-per-
238 cycle value.⁸ Under ideal self-limiting conditions, the character-
239 istic growth-per-cycle value would remain constant within a
240 certain temperature range (ALD window) where no thermal
241 decomposition takes place. For certain materials, the conven-
242 tional thermal ALD process at substrate temperatures lower
243 than precursor decomposition does not result in any film
244 deposition. In such cases, plasma-assisted deposition might
245 help in lowering the deposition temperature with the help of
246 energetic coreactant radical species.¹⁰⁴ The main drawback or
247 risk with plasma-ALD is the possible plasma damage, which
248 might be particularly significant for polymeric templates
249 including electrospun nanofibers. Figure 3 shows a unit

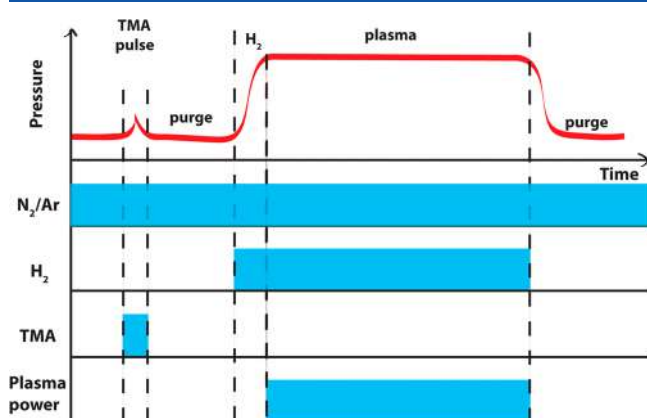


Figure 3. Temporal process layout for a unit plasma-ALD cycle of AlN and the corresponding variation of the reactor pressure over time. Initially, TMA pulse is introduced into the chamber onto the substrate, which is then adsorbed forming a monolayer. The excess precursor is pumped out. Then reactive N_2/H_2 plasma species are introduced to the surface which react with the adsorbed TMA to form AlN via ligand-exchange surface reactions. Then unreacted N_2/H_2 plasma radicals are purged out of the system to prevent subsequent gas-phase reactions. Reproduced from ref 105. Copyright 2019 American Vacuum Society.

250 plasma-ALD process cycle for AlN, with the precursor
251 (trimethylaluminum-TMA) and plasma coreactant ($N_2/H_2/$
252 Ar) exposure events separated by N_2/Ar -purge cycles and how
253 these process steps affect the reactor pressure during the
254 growth experiment.¹⁰⁵

255 **Up-Scaling.** For the up-scaling of ALD toward industrial-
256 scale high-volume production, deposition rates need to be
257 increased while not sacrificing from the ideal uniformity and
258 conformality. The growth-per-cycle (GPC) parameter in ALD
259 processes is pretty fixed and range typically within 0.5–2.0 Å;
260 however, the total time needed to complete the unit ALD cycle
261 might be further reduced with reactor and precursor pulsing
262 designs. Particularly, “spatial ALD” features dramatically

increased the deposition rates where the substrate is physically
moved in the spatial domain rather than waiting for purging
the active species out of the chamber in the time domain.
Using spatial ALD, orders of magnitude higher growth rates
have been achieved for several materials. Spatial ALD,
therefore, can in principle be applied for the ALD coating of
electrospun nanofiber templates as well as where the additional
precursor diffusion step needs to be incorporated. Further-
more, as the polymeric nanofibrous templates can be woven on
flexible substrates, even roll-to-roll ALD processes might be
feasible to develop which might further reduce the unit
production cost of such ALD-coated nanofiber materials.

Advantages. (1) Thermal ALD yields a very good
conformality over large surface areas, (2) scalable up to
industrial levels for high-volume production, (3) wide range of
inorganic materials toward various application interests can be
produced, and (4) novel precursors can be designed and
synthesized which might be used for alternative surfaces,
materials, and applications.

Disadvantages. (1) Possible chemical reactions between
the polymer nanofibers and the ALD-precursor may limit the
applicability. As a result, the interface may not be well-defined.
(2) Due to the directionality of the plasma-ALD, it requires
protective coating on the polymeric template. The plasma-
assisted ALD may not yield a uniform coating on the high
surface area nanofibrous templates. (3) ALD is limited by the
availability of the gaseous precursors with sufficient vapor
pressure and high thermal stability.

Hardware and Cost of Ownership. Practically any well-
designed ALD reactor, either thermal or plasma-assisted ALD
systems are sufficient to provide uniform and conformal
coatings on nanofibers or nanoparticle templates. The main
requirement is the ALD recipe which will allow the precursor
and coreactant molecules to diffuse freely within the
nanotemplate. To achieve this condition, conventional thin-
film coating ALD recipes are further modified with extra
“waiting periods” after the precursor/coreactant molecules are
pulsed into the reactor chamber. Typically, for flat substrate
coating experiments, the precursor/coreactant pulsing is
followed by an immediate N_2/Ar purging step, without any
need for an additional waiting period. For nanofiber/
nanoparticle template coating experiments, depending on the
effective surface area of the template, additional diffusion
periods of 30–180 s are utilized to ensure complete coverage
of all available surfaces. On a side note, although we mentioned
that plasma-ALD can provide conformal coatings as well, it is
also known that plasma processes exhibit inherent direction-
ality due to the directional flow of energetic radicals and ions,
which might result in reduced conformal coating performance.
In our work,^{54,55} we have demonstrated AlN and GaN coated
nanofibers via plasma-assisted ALD with decent (but not
perfect) conformality. Our thermal-ALD coated nanofibers
exhibited much improved conformality, as no directional
coreactants are present in thermal-ALD experiments. Never-
theless, plasma-ALD recipes can be tuned and adjusted to
show enhanced conformality, mainly by optimizing the reactor
pressure and the related radical residency times within the
reactor chamber.

Cost of commercial ALD reactors are typically of less or
equal (if heavily equipped with in situ metrology tools) value
when compared to widely used PVD systems like sputtering
and of significant lower cost when compared to epitaxial
growth reactors including MOCVD and MBE. On the other

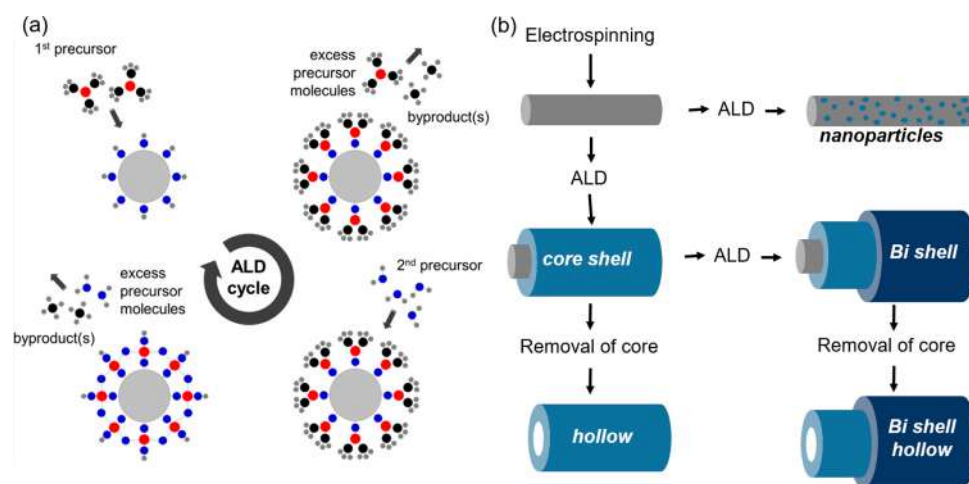


Figure 4. (a) Schematic representation of a unit ALD cycle and (b) electrospun nanofiber-based synthesis of nanostructures. Inorganic nanoparticle coated core–shell, bishell, hollow, and bishell hollow nanofibers. To prepare these nanostructures, we start with a nanofiber template and a conformal deposition of required material takes place on top of the template. By selectively removing the organic template by calcination, the above listed nanostructures could be obtained. Part a is reproduced from ref 106 Copyright 2013 John Wiley and Sons.

326 hand, precursor materials are the main consumables for ALD
 327 coatings, which are typically expensive if purchased from a few
 328 available precursor vendors. This cost item can be reduced if
 329 such precursor materials can be synthesized in-house.
 330 However, for most of the applications including (photo)-
 331 catalysis, energy storage, gas sensing, passivation, and transistor
 332 fabrication, typically less-than 20 nm and in some cases just a
 333 few monolayer-thick coatings are needed, which makes ALD
 334 the only viable option with still relatively low operation cost. In
 335 this case, the ownership cost including the consumables further
 336 reduces as the expensive precursor can be used for the coating
 337 of a high number of samples.

338 ■ ELECTROSPINNING AND ATOMIC LAYER 339 DEPOSITION

340 The integration of electrospinning and ALD are schematized in
 341 Figure 4. Figure 4a shows the schematic of a typical unit ALD
 342 cycle with precursor dosing and purge steps on a representative
 343 nanofiber cross-section. Essentially, precursors are adsorbed at
 344 the surface in a sequence and they react to form a conformal
 345 coating. Figure 4b depicts steps involved in obtaining various
 346 types of one-dimensional fibrous nanostructures, such as
 347 nanoparticle-decorated, core–shell, bishell, and so on. It also
 348 indicates the optional calcination process to remove the
 349 nanofiber core, which converts the nanofibrous structures into
 350 hollow nanofibers.

351 **Challenges of Combining Electrospinning and**
 352 **Atomic Layer Deposition.** Several critical challenges exist
 353 for an ideal conformal and uniform coating process on
 354 electrospun nanofiber template.

355 (i) Tuning the recipe to provide sufficient precursor
 356 diffusion time: In contrast to conventional ALD recipes,
 357 to ensure ultimate conformality on the large effective
 358 surface area of the nanofiber template, substantially long
 359 diffusion time intervals have to be incorporated in the
 360 deposition cycle of the material of interest. In order to
 361 do this effectively, the gate valve of the reactor chamber
 362 is closed right before the precursor pulsing so that
 363 maximum amount of precursor vapor is available for
 364 diffusing into the porous nanofibrous template. During
 365 this diffusion period, the chamber pressure is increased

significantly mainly due to the pump isolation and
 continuous carrier gas flow. The increased chamber
 pressure might cause additional challenges in the reactor
 operation, where pressure gauges operate typically at
 lower pressures. This additional precursor diffusion step
 is increasing the unit ALD cycle significantly, resulting in
 extremely long deposition times.

(ii) Keeping the substrate temperature below polymer
 melting temperature: Despite being known as a low-
 temperature deposition process, the low-temperature
 compatibility of polymeric materials pose an additional
 upper limit in substrate temperature to be used in ALD
 experiments. Typical deposition temperatures lower than
 150 °C work for most of the polymers and ALD
 materials. However, some compounds might require
 higher temperatures for deposition, which would
 contradict with the temperature limits of the polymeric
 material used in electrospun nanofibers. In such a case,
 an alternative to further reduce the deposition temper-
 ature would be to employ plasma-ALD at the expense of
 possible plasma damage and reduced conformality. As an
 example for this solution approach, we have successfully
 synthesized AlN coatings on polymer nanofibrous
 templates by reducing the typical thermal-ALD temper-
 ature from ~350 °C to less than 200 °C by using
 plasma-ALD. Due to the reduced deposition temper-
 ature, we were able to preserve the volumetric fibrous
 structure and obtain hollow nanofibers after the
 calcination process.

(iii) For plasma processes, to avoid plasma etching of the
 polymeric templates by energetic plasma species,
 protective layers should be used: Although being useful
 in reducing the ALD deposition temperature for
 compound materials, plasma processing comes with
 several critical shortcomings as well. First, the plasma
 damage factor might be severe for relatively easy to
 damage/etch polymeric materials. A possible direct
 mitigation measure for the plasma damage might be to
 reduce the rf-plasma power to minimize the incident
 energy of plasma species and to increase the chamber
 pressure in order to increase the number of collisions of

407 plasma species, thereby again decreasing the energy of
408 impinging plasma particles. Another indirect mitigation
409 technique that can be used to protect the polymeric
410 materials from degrading under plasma exposure is to
411 use protective layers on the surface of electrospun
412 nanofibers. Such protective conformal layers can be
413 deposited within the same ALD reactor, prior to the
414 plasma deposition process in thermal-ALD mode. Our
415 group has extensively employed this methodology for
416 the fabrication of flexible and hollow-core III-nitride
417 nanofibers. Another significant drawback of plasma-ALD
418 stems from the directional character of plasma processes:
419 this mainly results in a nonideal conformal coating on
420 high surface area nanoporous templates. This effect
421 might be reduced to a certain degree by increasing the
422 pressure inside of the chamber; however, the con-
423 formality performance would definitely not be as good as
424 thermal-ALD processes.

425 ■ PHOTOCATALYSIS

426 The photocatalytic performance of the nanostructures is
427 explored over the degradation of organic pollutants under
428 UV to visible irradiation. The energy of the illumination is
429 mainly determined based on the band gap of the catalyst;
430 however, defects within the band gap could be activated with
431 relatively lower energy. Typically,¹⁰⁸ 10 mg of the catalyst is
432 immersed in 25 mL solution of methyl orange (10 mg/L). For
433 UV radiation, a 400 W light source with an emission
434 wavelength range of 300–400 nm is employed for the
435 experiments. The light source is kept at a distance of 10 cm,
436 and the solution is kept under UV light for 3 h. A certain
437 amount of sample is collected and centrifuged to eliminate the
438 catalyst (if required), which is then subjected to UV–vis
439 transmission spectroscopy. By tracing the intensity of a
440 characteristic peak of the dye molecule with respect to UV-
441 exposure time, the concentration of the dye molecules is
442 calculated. The photocatalyst is fabricated by depositing
443 catalytically active material (metal oxide semiconductor) on
444 top of the electrospun fibers. Wide band gap metal oxide
445 semiconductors, such as ZnO and TiO₂ and their combina-
446 tions, were employed in different forms like core–shell,
447 nanoparticles, or nanoclusters. They are mostly tested for
448 catalytic activity through the photodegradation of organic
449 molecules (methylene blue, rhodamine B, methyl orange, etc.)
450 in water. The degradation produces CO₂ or H₂O with O₂ and
451 various molecular fragments.

452 Comprehensive reviews on semiconductor based photo-
453 catalysts have appeared in the literature.^{115–117} Various studies
454 on the photocatalytic applications of metal oxide coated
455 electrospun fibers have been studied by our research group by
456 combining electrospinning and ALD.^{4,35,45,46,68,82,109,118,119} In
457 a typical example, core–shell nanofibers were produced where
458 the core is nylon nanofibers while the shell is ZnO
459 nanoparticles or nanolayers.¹⁰⁹ As described earlier, a control
460 on the thickness of the shell layer is achieved by varying the
461 number of cycles in the ALD process. Hence, a transition from
462 nanoparticles to a nanolayer with a thickness of ~27 nm is
463 achieved. The highest photocatalytic activity (PCA) was
464 recorded when the nanoparticles densely cover the surface of
465 the nanofibers, and the activity decreases as the density of the
466 nanoparticle decreases. The enhanced catalytic activity was
467 attributed to their higher catalytic surface area that increases

the active sites.¹⁰⁹ We have further investigated the influence of
468 surface area of a semiconductor layer on the photocatalytic
469 performance,^{109,119} where we varied the mean diameter of the
470 core nanofiber (~80, ~240, and ~650 nm) and keeping the
471 thickness of the shell layer fixed (~90 nm). The morphological
472 and structural integrity were also investigated, and it is found
473 that ZnO is polycrystalline with a hexagonal wurtzite structure.
474 The nanofibers with the smallest mean diameter showed the
475 highest catalytic performance owing to their higher surface
476 area.¹²⁰ Also, the sample could be reused without any
477 significant decay in their PCA. Furthermore, we have improved
478 the catalytic activity by growing ZnO nanoneedles (diameter,
479 ~25 nm and the aspect ratio of ~24) using the hydrothermal
480 method on the surface of the nanofibers.⁴ These hierarchical
481 nanostructures depicted an enhanced catalytic performance
482 which was credited to the surface defects, while the needle
483 structure supports the vectorial transport of photogenerated
484 charge carriers. In connection to thd defects, we have studied
485 the intrinsic defect reorganization in ZnO and its effect on the
486 photocatalytic performance with hollow ZnO nanofibers.⁴⁵
487 ALD of ZnO with an average grain size of ~20 nm is obtained
488 on nanofibers of two different average diameters (80 and 650
489 nm). The results revealed that increasing the surface area does
490 not enhance the photocatalytic performance, rather the density
491 of the surface defects play a crucial role. In the first glance, it
492 might appear that the defect density is higher if the surface area
493 is increased. However, indeed, there is a critical balance that
494 one has to hit to obtain the highest PCA. Beyond a limit, the
495 increased density of defects decreases the electronic quality,
496 which decreases the quantum efficiency (photon to electron
497 conversion ratio). Clearly, we need to optimize the electronic
498 properties to obtain the highest performance. One of the ways
499 to tune the electronic properties is “doping”. Nasr et al.¹²¹
500 compared the PCA of Al₂O₃ doped ZnO nanotubes with that
501 of undoped ZnO. By changing the deposition sequences of the
502 Al₂O₃ and ZnO cycles, Al₂O₃ doped ZnO nanotubes with
503 different ratios of Zn/Al were produced. This is rather a
504 potential technique to produce doped semiconductor to
505 increase the carrier concentration. Under UV irradiation, the
506 PCA increased with increasing the ratio of Al₂O₃/ZnO.
507 Moreover, the nanotubes could be reused four times without
508 any significant decrease in the catalytic activity. Al₂O₃ doping
509 of ZnO can indeed decrease the resistivity and increase the
510 carrier concentration.¹²² A higher carrier concentration might
511 have increased the catalytic activity. This method could be
512 applied to other semiconductors. Despite TiO₂ being another
513 important large band gap material, doped counterparts using
514 ALD are not widely tested for the PCA. By giving the stability
515 and applicability of TiO₂, it is certainly a vital testing that still
516 needs to be addressed.

517
518 Another important strategy to obtain higher PCA is to delay
519 the recombination process of photogenerated electron–hole
520 pairs through an internal electric field that arises due to band
521 alignment. Szilagyi et al. reported WO₃/TiO₂ core (140–300
522 nm)–shell (1.5, 3.1, 10, and 19.3 nm) nanofibers and explored
523 their PCA¹¹³ with UV–vis or visible illumination only. The
524 nanofibers with 1.5 nm of the TiO₂ layer showed the highest
525 visible light catalytic activity. Catalytic activity is brought into
526 the visible region through the WO₃ core, where the visible light
527 can penetrate through the thin and wide band gap TiO₂ shell.
528 The smart design of structuring wide and smaller band gap
529 materials as shell and core, respectively, is notable. Also, TiO₂
530 is relatively a more stable material under photocatalysis. This

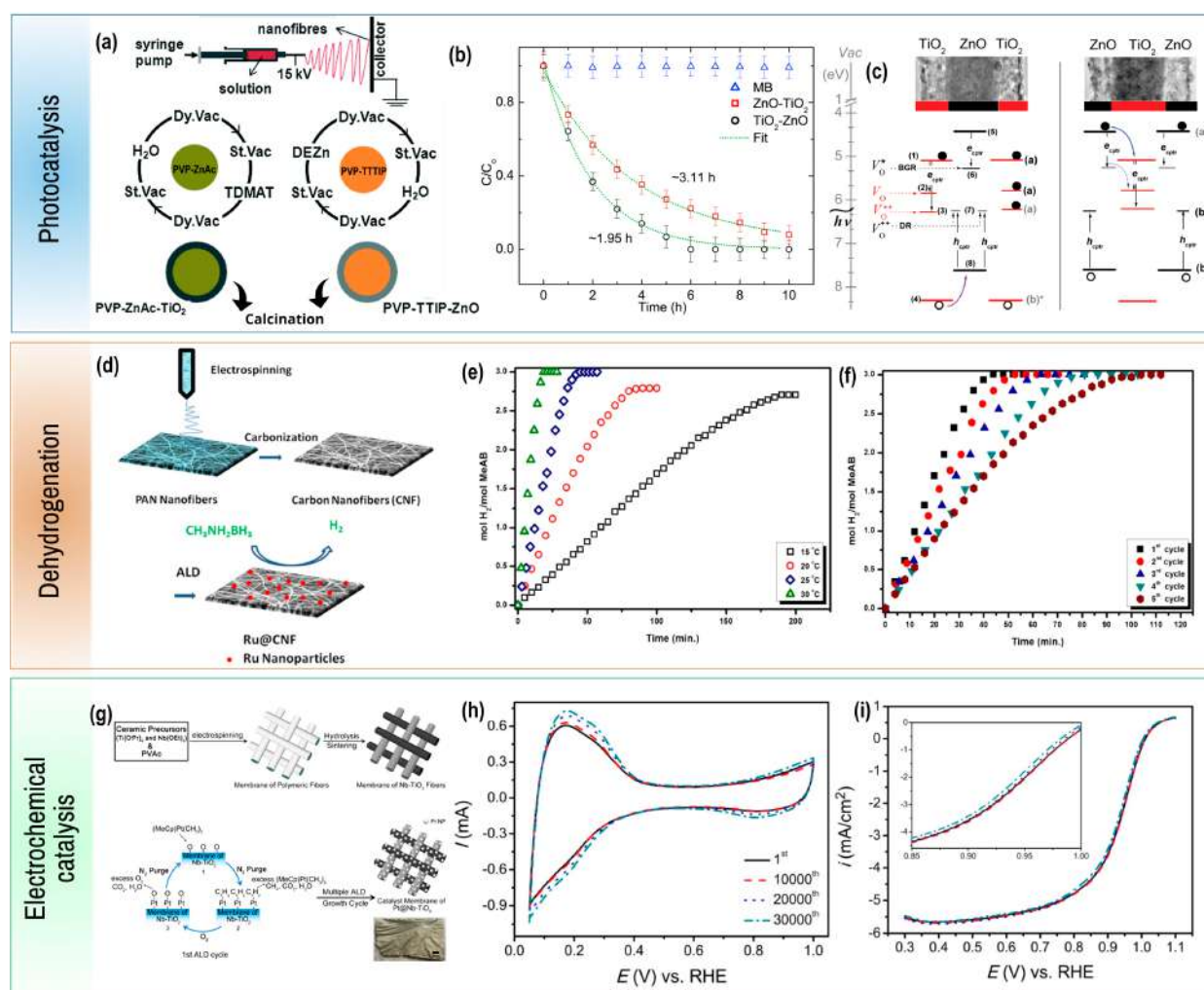


Figure 5. Applications of catalytic fibrous materials produced using both electrospinning and ALD. (a) Cartoon illustration of the production of core–shell heterojunction (CSHJ) nanofibers and (b) the PCAs of the ZnO–TiO₂ and TiO₂–ZnO core–shell heterojunction nanofibers. Constants and exponential decay fits are depicted with respect to the MB in the absence of a catalyst. (c) Proposed catalysis mechanism: electrons from the TiO₂ are engaged from the ZnO–TiO₂ CSHJ. The energetic band locations of TiO₂ were taken from the literature. (d) Cartoon illustration of the production of catalytic ruthenium (Ru) nanoparticle decorated PAN carbon nanofibers for MeAB dehydrogenation and (e) plot showing the mole of the formed H₂ per mole of MeAB versus time during the dehydrogenation of MeAB ($c_{\text{MeAB}} = 100 \text{ mM}$) catalyzed by Ru@CNF ($c_{\text{Ru}} = 0.0135 \text{ mM}$) at different temperatures, (f) plot depicting the mole of formed H₂ per mole of MeAB versus time for the 1st to 5th cycle in the Ru@CNF ($c_{\text{Ru}} = 0.0135 \text{ mM}$) catalyzing the dehydrogenation of MeAB ($c_{\text{MeAB}} = 100 \text{ mM}$) at RT. (g) Schematic illustration for the process for the fabrication of Pt@Nb–TiO₂ catalyst for ORR and the accelerated-stability test of Pt@Nb–TiO₂ catalyst having 10 at. % Nb: (h) cyclic voltammograms and (i) ORR polarization curves measured at 1600 rpm. First, second, and third rows of this figure were reproduced from ref 46 (Copyright 2014 Royal Society of Chemistry), ref 118 (Copyright 2018 American Chemical Society), and ref 134 (Copyright 2014 American Chemical Society), respectively.

531 protects the core-WO₃ material from degradation during the
 532 redox cycles. Santala et al. developed various approaches for
 533 the fabrication of catalysts.¹²³ Apart from hollow tube and core
 534 (NiFe₂O₄ or CoFe₂O₄)–shell structures, authors have
 535 synthesized hollow tubes filled with Fe₂O₃ nanoparticles,
 536 where the shell structure is always TiO₂.¹²³ The highest PCA
 537 was observed for Fe₂O₃ nanoparticle loaded TiO₂ nanotubes.
 538 Due to the presence of magnetic particles, the catalyst could
 539 easily be recovered from the solution and reused. When the
 540 catalyst is nonmagnetic in nature, centrifugation is the only
 541 quick recovery option if the structural integrity of the catalytic
 542 membrane is not good enough. The incorporation of the
 543 magnetic nanoparticles not only saves the recovery time but
 544 also makes the process easier. PCA of ZnO/ZnAl₂O₄
 545 multiconcentric nanotubes were studied.¹⁰⁸ In this case, the

core–shell nanofibers were subjected to two stage calcination. 546
 With increasing the number of layers, the formation of defects, 547
 stimulation of nonradiative recombination, and/or surface 548
 charge transfer took place in the structures, which significantly 549
 enhanced the PCA. So far, it is clear that the electrons and 550
 holes take part in the PCA; however, the individual role of 551
 each of the excited state carriers in the catalysis is not known. 552
 In this direction, our group has employed a core–shell 553
 heterojunction nanostructure based on TiO₂ and ZnO that can 554
 selectively expose either of the charge carriers to the 555
 environment (Figure 5a–c).⁴⁶ Given the band alignment 556
 between the core and shell materials, electrons or holes are 557
 selectively exposed to the catalytic environment under 558
 appropriate illumination (Figure 5c). Essentially, when the 559
 shell is TiO₂, electrons remain in the conduction band of TiO₂ 560

561 while the holes may migrate to the valence band of ZnO. The
562 electrons in the conduction band when available at the surface
563 take part in the catalysis process. The converse is true if the
564 shell layer is ZnO and the core is TiO₂. Indeed, these kinds of
565 catalysts must be tested for other synthesis applications where
566 one requires predominantly electrons or holes in the reactions
567 Apart from the excited state carriers, the defects at the surface
568 also play a crucial role in determining the rate of PCA. At the
569 TiO₂ (ZnO) surface, electrons (holes) from the conduction
570 (valence) band may be captured by oxygen vacancies. We
571 found that the catalytic activity is 1.6 times higher when holes
572 are involved in the catalytic activity, i.e., TiO₂–ZnO core–
573 shell heterojunction where lower mobility of holes and oxygen
574 vacancies play a crucial role.⁴⁶ In the case of the TiO₂–ZnO
575 core–shell heterojunction, the defect bound electrons and
576 holes take part in the catalytic reaction, where the efficiency is
577 limited by the recombination time-scale and their availability at
578 the surface. The energy from the defect electrons could be
579 captured, as shown by Aslan et al. with Pd/ZnO/polyacryloni-
580 trile nanofibers.³⁵ In their study,³⁵ anisotropic Pd nanocubes
581 were attached by submerging the nanofibers in the dispersion
582 of Pd nanocubes for 30 min and drying at 110 °C for 5 min.
583 Pd/ZnO nanofibers depicted better performance than that of
584 ZnO nanofibers, which was attributed to both energy transfer
585 between the Pd nanocubes and the ZnO nanolayer and
586 plasmonic resonance excited by the defect electrons of the
587 ZnO layer.³⁵ The basic idea of capturing the photoexcited
588 electrons and deploying them for PCA can be extended to
589 other material combinations including noble metals such as
590 Au. Also, these noble metals can increase the applicability by
591 taking part in metal catalyzed chemical reactions. Bechelany et
592 al. reported the preparation of metal organic framework
593 (MOFs) and projected their possible use in photocatalysis,
594 where ultrathin oxide (40–50 nm thick ZnO and Al₂O₃) layers
595 on PAN nanofibers were subjected to microwave-assisted
596 solvothermal treatment.⁷⁰ The characterization of the final
597 product revealed a specific surface area of $S_{\text{BET}} = 1760 \pm 260$
598 m² per gram while ZnO deposited PAN nanofibers have a
599 specific surface area (S_{BET}) of 10 m²/g. As discussed earlier,
600 increasing the surface area of the catalyst is a vital task, where a
601 balance needs to be achieved with respect to the surface
602 defects so that the overall optical quality of the catalyst is not
603 compromised. MOFs have grabbed serious research attention
604 which, however, is not thoroughly exploited for PCA with
605 hierarchical structure.

606 **Reduction, Dehydrogenation, and Hydrolysis Reac-**
607 **tions.** Chemical transformation of small organic molecules is a
608 rather important field of research, where nanostructures are
609 widely applicable as catalysts. This is due to their higher
610 specific surface area to volume ratio requiring a relatively
611 smaller quantity of the catalyst with respect to their bulk
612 counterparts. Celebioglu et al. studied the reduction of 4-
613 nitrophenol with core (polyacrylonitrile)–shell (TiO₂, 8 nm)
614 decorated with Pt nanoparticles (2 nm mean diameter).¹²⁴ It
615 found that the deposition of a thin layer of TiO₂ enhances the
616 stability of the polymer and improves the attachment of Pt
617 nanoparticles. Also, the nanofibers could be reused several
618 times without any significant change in the fiber morphology at
619 a degradation rate of 0.1102 s⁻¹. In a recent study, Pd
620 nanoparticles (~4 nm in diameter) are coated on top of cross-
621 linked cyclodextrin nanofibers and employed for the hydro-
622 genation of 4-nitrophenol.¹²⁵ Khalily et al. studied hydrolytic
623 dehydrogenation of methylamine borane (MeAB) with Ru/

carbon nanofibers.¹¹⁸ The electrospun PAN nanofibers were 624
carbonized and functionalized with Ru quantum dots of 3.4 ± 625
0.4 nm (Figure 5d). The volume of hydrogen quantifies the 626
catalytic activity which measured during the hydrolytic 627
dehydrogenation of MeAB (Figure 5e). In a control measure- 628
ment, Ru-free carbonized nanofibers depicted no catalytic 629
activity. The rate constants (k_{obs}) for the reaction were, 630
respectively, 0.00163, 0.0458, 0.0763, and 0.2033 mol H₂/(mol 631
MeAB × min) at 15, 20, 25, and 30 °C. Furthermore, the 632
activation energy (E_a) for the dehydrogenation of MeAB by 633
Ru@CNF was found to be 30.1 kJ/mol, which was much lower 634
than most catalytic systems reported in the literature. 635
Moreover, the catalytic stability of the Ru@CNF was evaluated 636
over five repetitive cycles, and the nanofibers could completely 637
convert the MeAB by retaining 72% of its intrinsic catalytic 638
performance even at the fifth recycle (Figure 5f). In another 639
study,¹²⁶ TiO₂ hollow nanofibers were used to grow MOFs on 640
the fibers through solvothermal synthesis. The resultant fibers 641
were tested for the hydrolysis of methyl paraoxon where the 642
formation of 4-nitrophenoxide was observed by monitoring the 643
UV–vis absorption band at 407 nm.¹²⁶ PVDF/Ti(OH)₄ and 644
PMMA/Ti(OH)₄ nanofibers were subjected to 200 ALD 645
cycles to form TiO₂. Then solvothermal synthesis was 646
employed for the synthesis of UiO-66-NH₂ crystals. During 647
the solvothermal process, the PMMA core was removed, 648
leading to hollow fibers, while the PVDF core remained. 649
Hollow fibers with MOF crystals have a specific surface area of 650
264 m² g⁻¹. Osman et al. produced catalytic PAN nanofiber 651
functionalized nanoparticles of ZnO and Pd nanocubes for 652
2,4,6-trinitrotoluene (TNT) reduction (nitro groups of TNT 653
into amine groups).¹²⁷ Pd nanocubes were coated on top of 654
PAN/ZnO nanofibers. Indeed, the catalysis using the 655
nanostructures is limited to the conversion of small molecules. 656
However, there is an explored and huge potential that exists 657
with these nanostructured catalysts. Not only is the advantage 658
limited to the high surface area to volume ratio, it extends into 659
the density of surface bound active sites, has easy recovery 660
from the reactants, and a combination of multilevel hierarchical 661
structures can be produced. If suitably explored, we speculate 662
that these catalysts find applications in biphasic interfacial 663
reactions, where the catalytic membrane at the interface 664
separates reactants and products into two different phases. 665
Since the surface functional groups determine the hydrophilic 666
and hydrophobic nature of the polymer, this could be a very 667
good starting point. 668

669 **Electrochemical Catalysis, H₂O Splitting.** Similar to 669
photocatalysis, the activity of (photo)electrochemical catalysis 670
crucially depends on the electronic properties of the catalyst in 671
conjunction with carrier-concentration and its chemical 672
potential with reference to the redox potential of water. It is 673
important that the stability of the catalyst depends on the 674
choice of the material where the chemical potential is an 675
intrinsic property. Our research group recently tested 676
NiOOH/Ni(OH)₂ decorated flexible carbonized PIM fibers.⁸² 677
The fibers showed a low onset potential ($\eta_{\text{HER}} = -40$ and $\eta_{\text{OER}} = 290$ 678
mV vs RHE), small overpotential at η at 10 mA cm⁻² 679
(hydrogen evolution reaction (HER) = -147 mV and oxygen 680
evolution reaction (OER) = 390.5 mV), outstanding kinetics 681
(Tafel slopes for HER = 41 mV dec⁻¹ and OER = 50 mV 682
dec⁻¹), and high stability (>16 h) for water splitting in 0.1 M 683
KOH. MWCNT/TiO₂ nanofibers were also tested,¹²⁸ where 684
the current densities were found to be 5.1, 4.4, 2.6, 1.7, and 1.0 685
mA/cm² for 20, 10, 5, 2, and 0% of MWCNT in TiO₂, 686

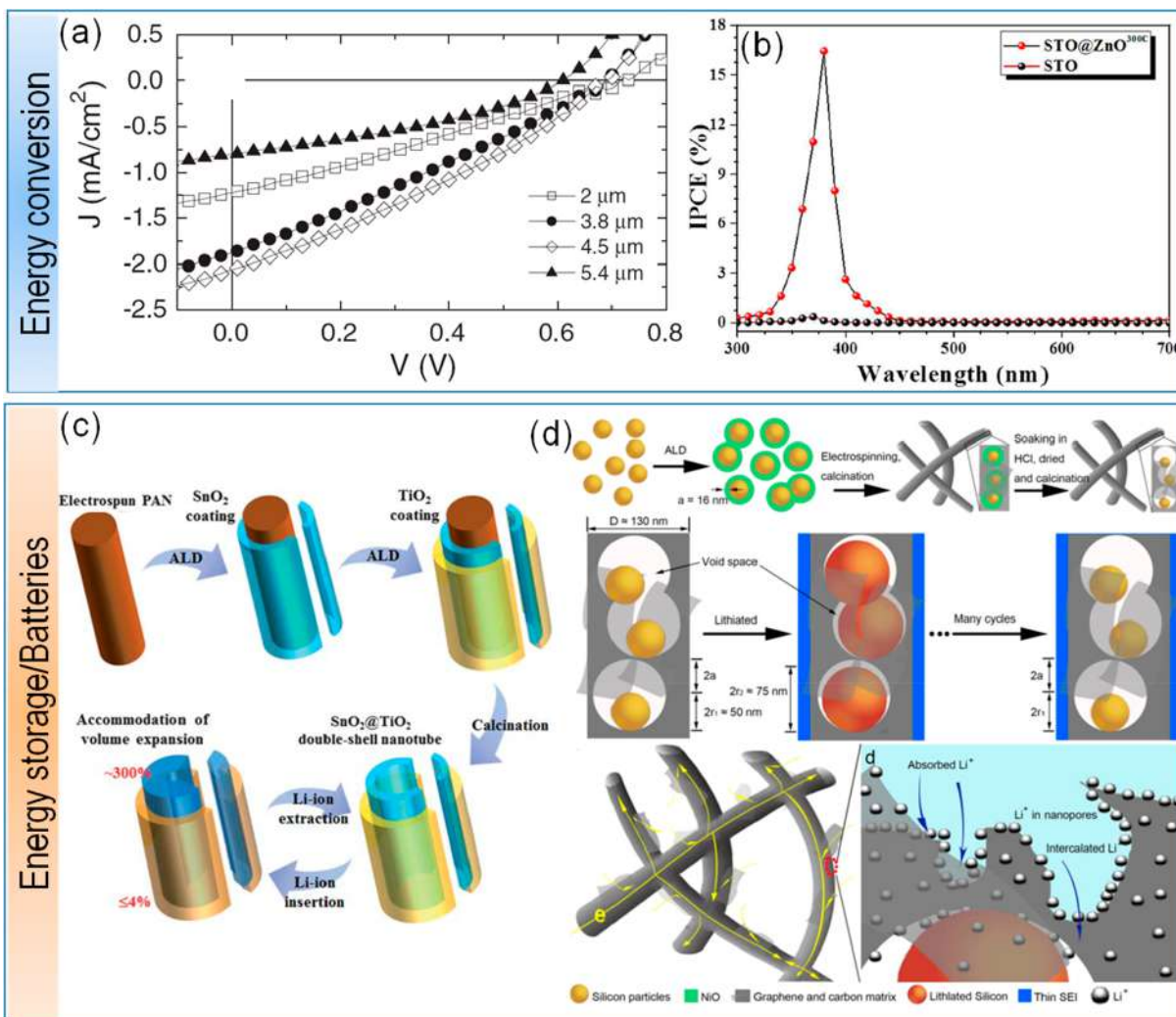


Figure 6. (a) J - V characteristics of TiO₂ nanofiber devices with four different TiO₂ nanofiber layer thicknesses, from 2 μm (open square), to 3.8 μm (solid circle), to 4.5 μm (open diamond), and to 5.4 μm (solid triangle). (b) Incident photocurrent conversion efficiency (IPCE) curves for the bare SrTiO₃ (STO) and STO@ZnO^{300C} photoanodes, where ZnO^{300C} indicates 300 cycles of ALD of ZnO on STO fibers. The presence of ZnO promotes the photon absorption and collection via the bandgap transition of STO. In addition, the IPCE reached a maximum of ~16.43% at ~380 nm for the STO@ZnO hybrid photoanode, which is ~44 times to that of bare STO at ~370 nm (i.e., ~0.37%). (c) Schematic diagram depicting the synthesis of the SnO₂/TiO₂ double-shell nanostructure and lithium-ion insertion and extraction. Polyacrylonitrile nanofibers were subjected to ALD of SnO₂ and then TiO₂. The TiO₂ outer shell maintains the structural integrity of the electrode during the charge–discharge cycles, where significant internal stress is expected due to the volume expansion. In fact, the hollow nature accommodates the volume expansion. (d) Synthesis and design of the 3D FSiGCNFs. (top row) Illustration of the synthesis process of the 3D FSiGCNFs. The 3D FSiGCNFs were soaked in hydrochloric acid solution to remove the NiO to form precise and controllable expansion space and annealed at 800 °C in Ar atmosphere for 2 h. (middle row) Schematic diagram of the 3D FSiGCNF electrode design. Rationally designed FSiGCNFs with precise control of the expansion space by ALD, followed by electrospinning, were used as protection of Si NPs for flexible and binder-free lithium-ion batteries. The graphene/carbon matrix with excellent mechanical strength and electron transport properties not only achieves a superfast electron transfer but also provides enough space to buffer the volume changes of Si NPs during the lithium insertion and extraction reactions. In addition, the stable SEI forms outside of the graphene/carbon matrix rather than on the surface of Si NPs, which is attributed to the electrolyte being blocked by the hierarchical porous graphene/carbon matrix, while facilitating lithium transport throughout the whole structure. The 3D FSiGCNFs can keep the overall morphology, and the SEI outside the graphene/carbon matrix is not ruptured and remains thin after deep electrochemical cycles. Illustration of (bottom row) electron transmission and Li⁺ storage in the 3D FSiGCNF film. Parts a, b, c, and d are reproduced from ref 36 (Copyright 2013 Elsevier), ref 67 (Copyright 2018 Royal Society of Chemistry), ref 56 (Copyright 2013 Royal Society of Chemistry), and ref 44 (Copyright 2016 American Chemical Society), respectively.

687 respectively. Doping of a semiconductor increases the carrier
 688 concentration and may introduce in gap states that could be
 689 used for visible light harvesting. ALD is a very promising
 690 technique for doping the wide band gap semiconductors, and a
 691 large scope is visible for future development of the catalysts for
 692 water splitting. Nitrogen doping of TiO₂ is one such
 693 example.¹²⁹ After doping, the hydrogen evolution capability

and a 10-fold improvement (0.09 to 0.8%) were observed in
 the photoconversion efficiency. Du et al. reported niobium-
 doped titania-supported Pt catalysts (Pt@Nb-TiO₂).¹³⁰ First,
 niobium-doped titania (Nb-TiO₂) nanofibrous membrane was
 produced using poly(vinyl acetate), titanium(IV) isopropoxide,
 and niobium ethoxide (Figure 5g). The nanofibers were
 pyrolyzed in air at 500 °C for 24 h to yield Nb-TiO₂ fibers. 700

After the deposition of Pt nanoparticles of various sizes (depending on the applied ALD cycle), Pt@Nb-TiO₂ fibers were tested for the oxygen reduction reaction (ORR). The area-specific ORR activities of the catalysts rose from 0.0084 to 0.28 mA/cm² for Pt@TiO₂ while it reached 0.9 V (vs RHE) when doped with 10 at. % Nb (Figure 5h,i). The accelerated-stability test on the Pt@Nb-TiO₂ revealed a very high stability with ~10% loss in activity. Recently, Khalily et al. reported Co₃O₄ nanocrystals (~3 nm mean diameter) decorated with nitrogen doped carbon nanofibers for ORR and oxygen evolution reactions (OER).¹³¹ An onset potential of 0.87 V with a Tafel slope of 119 mV dec⁻¹ was observed, which is close to the performance of a commercial Pt/C catalyst. The turnover frequency value was calculated at an overpotential of 550 mV to be ~0.14 s⁻¹, which is ~15 and 3-fold higher than those of the standard IrOx (0.0089 s⁻¹) and bulk Co (0.05 s⁻¹) catalysts. Further on, with the carbon nanofiber electrodes, recently, self-supported electrodes with Ni/NiO and Pd nanoparticles are employed for HER/OER.¹³² The best CNF-Ni/NiO-Pd electrode displayed the lowest overpotential (63 mV and 1.6 V at $j = 10$ mA/cm²), a small Tafel slope (72 and 272 mV/dec), and an exchange current density (1.15 and 22.4 mA/cm²) during HER and OER, respectively. Notably, these electrodes consist of graphitic layers that cover and protect the Ni/NiO NPs from corrosion. Photo/electrochemical activity of the TiO₂ surface is already well known. Indeed, TiO₂ coated poly(acrylonitrile) fibers were employed for HER through biological species, viz, *Escherichia coli*.¹³³ The TiO₂ coated membranes were then functionalized with a [NiFe]-hydrogenase-containing membrane fraction from *Escherichia coli*. This hierarchical structure generates an organic film around the fiber mat which depicts the electrochemical activity for HER, where the current densities were more than 500 mA/cm² at 0.3 V overpotential.

ENERGY: GENERATION AND STORAGE

One of the methods to convert renewable energy to electric power is deploy solar cells. Li et al.³⁶ compared the photovoltaic device performances of the FTO/TiO₂-HBL/TiO₂-nanofibers-dye/P3HT/PEDOT:PSS/Au device structure, where TiO₂-HBL (hole blocking layer) is prepared via ALD or spin-coating. Pinhole free structurally integral ALD-TiO₂ film depicted a relatively higher efficiency, due to reduced dark leakage current and increased charge carrier lifetime. See Figure 6a for JV curves from this DSSC. A number of studies employed electrospun nanofiber as active junction material, especially in dye sensitized solar cells (DSSCs). The applicability of electrospun nanofibers is due to the high surface area to volume ratio. However, the morphology that results from electrospun nanofibers consists of a large density of grain boundaries where the generated charge carrier could be trapped. This trapping could be detrimental for the efficiency of the device. Notably, the conformal coating that could be obtained from ALD is least explored when combined with the electrospun nanofibers. Much of the research focus is needed on how to reduce the grain boundaries through the ALD.

Apart from solar cells, photoelectrochemical splitting is another methodology to produce energy. As discussed earlier in the section Photocatalysis, impeding the e/h recombination is essential for higher catalytic activity. Similarly, it is the case with photoelectrochemical activity. For instance, the internal electric field between SrTiO₃ (STO) nanofibers and ALD

coated ZnO film hindered the e/h recombination and enhanced the photoelectrochemical activity. This heterojunction, depicted a promising photocurrent stability of ~61.3 μ A/cm², which was ~600 times higher than that of the pristine STO homojunction counterpart (0.12 μ A/cm²).⁶⁷ See Figure 6b for incident photon-to-current conversion efficiency with reference to the wavelength.

Energy that has been produced from the renewable natural sources (solar energy, wind energy) needs to be stored in the form of electrochemical energy with the help of batteries and supercapacitors. Earlier investigations³⁷⁻⁴⁴ aim at the development of new and next generation electrochemical energy storage technologies due to the ever increasing demand for energy. Over the current trend, lithium-ion batteries are promising power storage devices in the smart and portable electronic devices due to relatively higher specific power density which is rather an important factor for commercialization. This is where the high surface area to volume ratio of nanofibers plays a crucial role which can support higher current densities with three-dimensional architecture.

Generally, the development is focused on the construction of a new set of electrode materials or assemblies to produce efficient, stable, and cost-effective energy storage applications, where highly efficient electrochemical activity, shorter ionic path, and high electrical conduction are efficiency determining factors.⁴⁴ Commonly, graphite based electrode systems are used as an anode material in lithium-ion batteries due to higher stability, good electrical conductivity, and relatively lower cost. Alternative anode-materials such as MoS₂,³⁷ Sn,³⁸ Ge,³⁹ and carbon^{38,40,41} have also been studied for lithium and sodium ion batteries.³⁷⁻⁴³ To improve the storage-efficiency, it is crucial to design a hierarchical nanoarchitecture, where the combination of electrospinning and ALD play a crucial role. Among the low-dimensional electrode materials, continuous 1D electrospun nanofibers have grabbed the attention as promising electrode materials with intriguing properties when compared with the electrode systems synthesized through other approaches. Also, electrospun nanofibers have an additional advantage such as scalability.²⁷ Readers are encouraged to go through a comprehensive review that covers the secondary batteries based on electron spun nanofibers.²⁷ The most important role of ALD, in this case, is to produce highly conformal coatings (TiO₂,^{38,39} Al₂O₃^{41,42}) that not only protect the active material from pulverization, cracking, etc. but also changes the surface functionality to the hydrophilic nature enhancing the electrolyte uptake. Furthermore, the TiO₂ layer inhibits the reactions with lithium or sodium and enhances the stability of the electrodes. On the other hand, Ru⁴⁰ and Sn,³⁸ like heavy metals, are deposited in the form of nanoparticles on the surface of the protective coating⁴⁰ or directly on top of the electrode,³⁸ which in both cases the conductivity of the electrode increases. Normally nanoparticles are aggregated which results in the unstable specific surface area. This instability lowers the overall performance of secondary batteries, where relatively high capacitance and long stability are compromised.

Jean et al.¹¹⁴ studied an electrode material based on TiO₂-SnO₂-TiO₂ trilayered tubular nanostructures. The electrode depicted high reversible stability of ~550 mA h/g even after 60 cycles at a current density of ~50 mA/g. The sandwich architecture accommodated the mechanical stress during the charge-discharge cycles and improved the electrochemical properties. On the other hand, SnO₂-TiO₂ double shell

826 nanotubes depicted stable and reversible capacity with higher
827 current density than that of single SnO₂ and TiO₂ nanotube
828 electrode assemblies.⁵⁶ Figure 6c shows a schematic of lithium
829 ion insertion and extraction. Electrospun Si-loaded carbon
830 nanofibers with alumina coating were tested for electro-
831 chemical performance, and it is found that alumina coating
832 increases the mechanical integrity, stability, and prevents any
833 unwanted reactions between electrode and electrolyte.¹³⁵ This
834 is where the conformality of ALD is apparent. Furthermore, as
835 expected, the thickness of the alumina determines the
836 resistance to the transfer of charge. Also alumina coating
837 improves the capacitance retention from 36.1% to 82.3% for 28
838 cycles of ALD when compared to that of uncoated Si/C
839 nanofibers. Zhu et al.⁴⁴ developed a flexible anode for lithium
840 ion batteries. In their report, a 3D architecture of flexible
841 silicon and graphene/carbon nanofibers (FSiGCNFs) is
842 studied where an atomic-scale control of the expansion space
843 is obtained without any binder. Figure 6d shows the detailed
844 schematic of the fabrication and ion exchange process. During
845 the charge–discharge cycles, Si nanoparticles depict volume
846 expansion, where in FSiGCNFs the Si nanoparticles are
847 surrounded by accurate and controllable void spaces. This
848 readily increases the structural stability where the void spaces
849 minimize any damage due to the volume expansion. This 3D
850 porous structure with built-in void space between the Si and
851 graphene/carbon matrix not only limits most solid electrolyte
852 interface formation at the outer surface, instead of on the
853 surface of individual NPs, and increases its stability. As a result,
854 highly efficient channels were produced for the fast transport of
855 both electrons and lithium ions during cycling. The electro-
856 chemical performance of FSiGCNFs is significant indeed, viz,
857 2002 mAh g⁻¹ at a current density of 700 mA g⁻¹ over 1050
858 cycles corresponding to 3840 mAh g⁻¹ for silicon alone and
859 582 mAh g⁻¹ at the highest current density of 28 000 mA g⁻¹.
860 A conformal coating of Sn on carbon nanofibers increased
861 the conductivity, while TiO₂ coating is employed as a
862 protective coating.³⁸ The pipe-wire form of TiO₂-Sn@carbon
863 resulted in relatively higher capacity. Also, more stable cycle
864 performances are recorded with both lithium (643 mAh/g at
865 200 mA/g after 1100 cycles) and sodium ion (413 mAh/g at
866 100 mA/g after 400 cycles) batteries. TiO₂ coated germanium
867 and graphene composites are tested for efficiency as anode
868 materials.³⁹ The specific capacity of TiO₂ coated composite is
869 1050 mA h/g (100th cycle) and 182 mA h/g (250th cycle) for
870 the lithium and sodium ion batteries, respectively. These values
871 have shown significant improvement from pristine germanium
872 and germanium/graphene nanofibers. Ru-nanoparticles/TiO₂
873 on nitrogen doped carbon nanofibers depicted higher mass
874 transport and electrical conductivity while Ru-nanoparticles
875 increased the round-trip efficiency.⁴⁰ Theoretical results
876 indicated that Ru and TiO₂ enhance the electron transport
877 capacity of Li₂O₂ when compared to that of pristine carbon
878 nanofiber network. Among TiO₂/MoS₂ and pristine MoS₂
879 nanofibers,³⁷ the latter depicted an efficient discharge
880 capacitance of 840 mA h/g² at the second cycle and the
881 excellent rate capacity than that of bulk MoS₂. Also, ~30%
882 retention capacity is observed. Here, ~4 nm of TiO₂ film
883 protects the sulfur dissolution during the cyclic process;
884 however, the authors observed some reduced storage
885 capacitance and increased retention (up to ~64%) after 30
886 cycles. Apart from the expensive lithium based battery
887 technologies, sulfur-based systems have been tested owing to
888 the advantages of lower cost, acceptable energy density, and

sustainability.^{41,43} Fe₂O₃-carbon nanofibers were subjected to 899
vapor phase sulfidation at 600 °C under vacuum to produce 890
FeS₂-carbon nanofibers for Li-S batteries (electrolytes: conven- 891
tional carbonate electrolyte and a “solvent-in-salt”-type).⁴¹ Due 892
to vacuum and thermal processing, the electrode surface is now 893
binder-free and depicted a cycling stability (working voltages 894
with reference to Li/Li⁺) of 1.5–3.0 V with carbonate 895
electrolyte and in solvent. When the surface is coated with 896
50 nm of Al₂O₃ on the FeS₂-carbon nanofiber, the cycling 897
stability of the Li-FeS₂ system is increased to 1.0–3.0 V along 898
with the high discharge energy density at both the material 899
level (~1300 Wh/kg) and electrode level (~1000 Wh/kg). In 900
another example, porous C/BaTiO₃ nonwoven nanofibers 901
were initially stabilized at 280 °C for 4 h in air and then 902
carbonized at 900 °C for another 6 h at 2 K/min heating rate 903
under N₂ atmosphere. Then the porous C/BaTiO₃ mats were 904
treated with sulfur powder (heated to 160 °C for 10 h under 905
vacuum and then raised to 260 °C for 1 h in an Ar-filled 906
tubular furnace) followed by ALD coating of TiO₂. The 907
heterostructure depicted discharge capacitances of 524.8 and 908
382 mA h/g after 1400 at 1 A/g and 3000 cycles at 2 A/g, 909
respectively. This results from the inhibition of the volume 910
expansion and shuttle effect, effective utilization of the active 911
material, and formation of an interface with stable ionic 912
transport channels. Yan et al.³ compared various methods of 913
synthesis of V₂O₅ and found that the electrospun V₂O₅ 914
nanofibers depicted relatively higher specific capacitance of 915
190 F/g in aqueous electrolyte (2 M KCl) and 250 F/g in 916
organic electrolyte (1 M LiClO₄) with energy densities of 5 917
Wh/kg and 78 Wh/kg, respectively.¹³⁶ The specific capaci- 918
tance is comparatively lower (150 F/g in aqueous electrolyte) 919
when V₂O₅ is loaded on top of a carbon fiber as a composite. 920
Also, the energy density turned out to be lower, viz, 18.8 Wh/ 921
kg.¹³⁷ With the lack of commercial devices, indeed application- 922
oriented process research requires more attention so that the 923
viable techniques such as electrospinning and ALD will lead to 924
a commercial device, however, with not undermining the 925
fundamental research. Notably, commercialization of such 926
energy storage devices requires multistage research on various 927
aspects. It is ideal to implement industrial research projects so 928
that the researchers while perusing a scientific idea would be 929
able to extend the thought process until the stage of 930
commercialization. 931

■ GAS SENSORS 932

The nanostructured form of hierarchical 1D assemblies of wide 933
band gap semiconductors such as ZnO,^{50,51,57,60,61,138–140} 934
SnO₂,^{65,111,140} TiO₂,^{50,51,57} including CuO (ref 112) depicted 935
unique surface functionalities and higher sensitivities toward 936
ethanol,¹³⁸ O₂,^{51,60,140} NO₂,^{57,60,65,139,140} CO,^{57,60,65,112,139} 937
NH₃,^{50,65} H₂,^{65,111} etc. The basic principle of gas sensing is 938
as follows. In the case of semiconductors, when the gas 939
molecule adsorbs at the surface, the free electrons (hole) in the 940
conduction band (valence band) may be captured by the gas 941
molecule and/or adsorbed at the defect. The shift of charge 942
can be partial or complete depending on the adsorbing species 943
and availability of the unoccupied states. Since the carrier 944
density is decreased upon adsorption, a change in the 945
conductivity could be expected. As the concentration of the 946
test gas molecule increases, the trapped charge density also 947
increases, thus the conductivity decreases. A calibration curve 948
is obtained by recording the change in the electrical 949
conductivity with reference to the concentration of the test 950

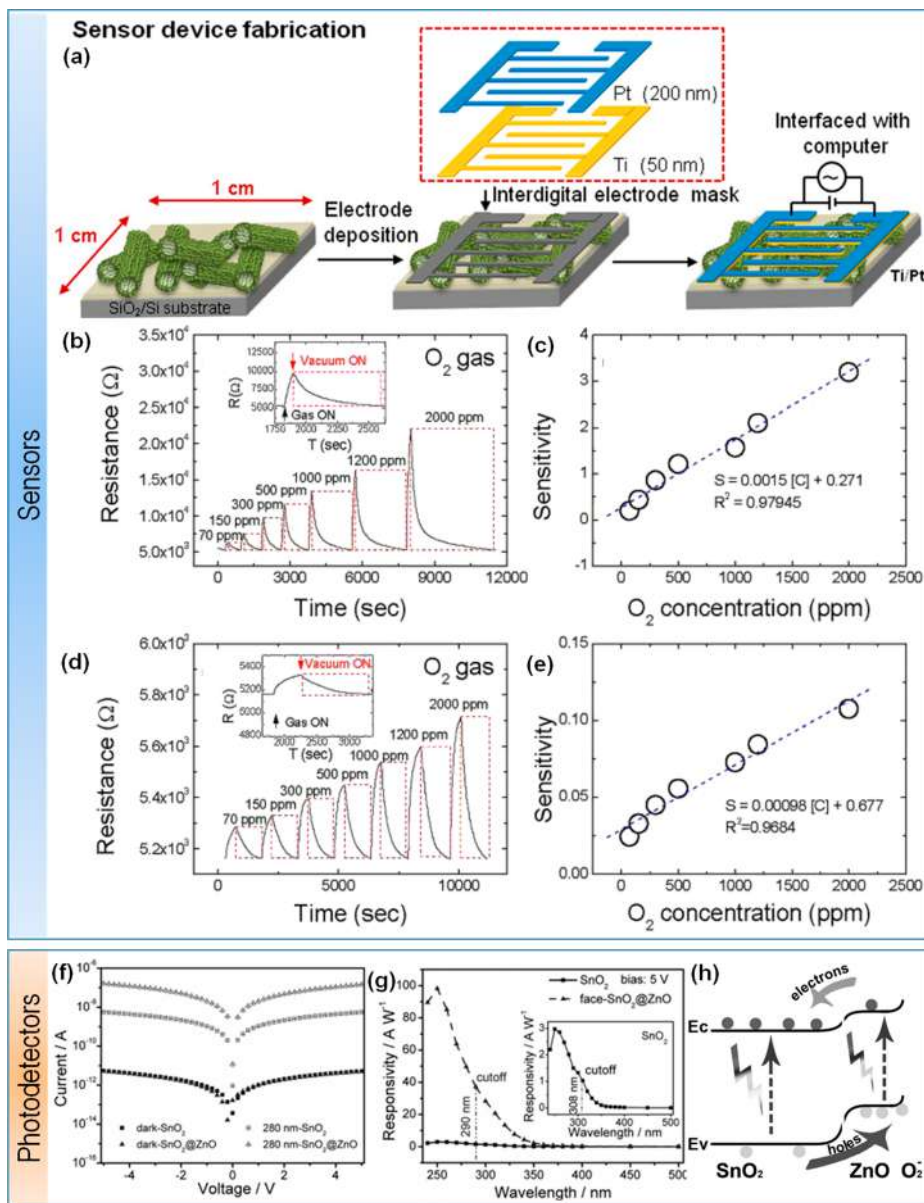


Figure 7. (a) Schematic process of fabrication of a sensor device with ZnO hollow fibers on SiO₂/Si. The interdigital electrode pattern Ti/Pt is deposited on top of ZnO hollow fibers. The electrical characteristics are recorded with reference to the concentration of the test gas. (b) Dynamic response of the ZnO nanofiber based sensor to O₂. The inset is the enlarged part of the data obtained at 300 ppm of O₂. (c) Variation of sensitivity as a function of O₂ concentration. Electro optical response of the Ω-shaped SnO₂@ZnO based photodetector is shown from parts f to h. (f) *IV* curves from the SnO₂ and SnO₂-ZnO under illumination of 280 nm wavelength light compared with that of the dark. The *IV* curves almost overlap across the two types of devices, while the photocurrent depicted a significant difference. The hybrid structure reaches 0.1 μA at 5 V. (g) Spectral responsivity is compared across SnO₂ and SnO₂@ZnO photodetectors. The hybrid detector is ~30 times more responsive than the pure SnO₂ counterpart with a shift of cut off wavelength to 290 nm from 308 nm. The observed improvements are attributed to their type-II band alignment and built-in electric field as shown in part h. Under UV illumination, electrons tend to move into SnO₂ while holes to the ZnO shell. Part a, parts b–e, and parts f–h are reproduced from ref 60 (Copyright 2014 Institute of Physics), ref 140 (Copyright 2009 Institute of Physics), and ref 53 (Copyright 2017 John Wiley and Sons), respectively.

951 gas, from which the sensitivity can also be calculated. A
 952 schematic of a typical gas sensor is shown in Figure 7a. Despite
 953 the whole process appearing to be simple, the dynamics of
 954 adsorption and desorption and the mechanism of sensing
 955 determine not only the selectivity and sensitivity but also the
 956 time-based response. Since the adsorption and desorption
 957 processes are required to take place sequentially, the sensors
 958 are operated at relatively higher temperatures.

959 Ethanol sensitivity is tested on the tubular assembly of ZnO
 960 nanostructures while varying the thickness of the shell and the

operating temperature.¹³⁸ The lower the thickness of the wall, 961
 the better the responsivity when tested within a thickness- 962
 range of 10–50 nm. Authors report that for a sample of a 10 963
 nm thick shell, the surface is completely depleted and thus they 964
 observed the highest response to the rest of the vapor at a 965
 sensing temperature of 450 °C. Further into the sensing, O₂, 966
 NO₂, and CO gases have been tested on ZnO nanotubes, 967
 where the sensitivity of the sensor to CO gas depends on the 968
 thickness of the shell,⁶⁰ however, better than that of ZnO 969
 nanofibers.⁶¹ The calcination temperature (determines its 970

971 crystallinity) at which the process of transforming the core–
972 shell nanofiber into the tube (sacrificial polymer core) also
973 plays a crucial role. The formation of nanograin assemblies in
974 the fiber-network is the key for higher sensitivity. Other
975 studies¹³⁹ have focused on the diameter of the nanotube (fixed
976 wall thickness of ~60 nm) on the sensitivity toward CO and
977 NO₂ exposure. At a critical thickness of the wall, high
978 selectivity is observed with CO gas over H₂, benzene, and
979 toluene gases. SnO₂ nanotubes were studied for sensitivity of
980 ethanol over H₂, CO, NH₃, and NO₂ gases,⁶⁵ where the
981 thickness of the shell wall has been varied from 8 to 37 nm.
982 Twisting the sacrificial PAN nanofibers and depositing the
983 SnO₂ layer resulted in SnO₂ nanotube microyarns.¹¹¹ A stable
984 and reversible H₂ response is obtained for a diameter of 500
985 nm and a wall thickness of 70 nm. The width of the depleted
986 and undepleted regions determine the change in the resistance
987 of the device and hence the sensitivity.

988 ALD of two different inorganic materials (TiO₂ and ZnO)
989 on a sacrificial electrospun nanofiber yields double layered
990 hollow nanofibers (see Table 1). These heterostructures were
991 tested for gas sensitivity with CO and NO₂ as a function of
992 thickness of the shell.⁵⁷ The results suggested that the double
993 layer hollow fibers were more efficient than that of hollow
994 fibers in terms of sensitivity toward reducing gases, however,
995 quite lower responses for oxidizing gases. Core–shell
996 structured TiO₂-ZnO nanofibers depicted better sensing
997 response toward NH₃ than that of ZnO-TiO₂ due to higher
998 sensitivity of the ZnO-shell.⁵⁰ On the other hand, SnO₂-ZnO
999 based core–shell nanofibers were tested for O₂ and NO₂
1000 sensitivities which performed better than pristine ZnO
1001 nanofibers.¹⁴⁰ The time-dependent response of SnO₂-ZnO in
1002 the presence of O₂ is shown in Figure 7b–e for various gas
1003 concentrations. Core–shell TiO₂-ZnO nanofibers were tested
1004 for O₂ sensing.⁵¹ When O₂ is adsorbed at the surface on the
1005 ZnO layer, the depth of the surface depletion layer changes
1006 and that is reflected in the resistivity. An ultrathin shell (~10
1007 nm) of ZnO on the SnO₂ nanofibers resulted in a notable
1008 sensing response and selectivity over their pristine counter-
1009 parts, where the selectivity was associated with the depletion
1010 layer at the surface.¹⁴¹ The improvement in the sensing
1011 performance may be attributed to the formation of a
1012 heterointerface, surface depletion layer and the internal electric
1013 field created at the interface. Core–shell structured CuO (*p*-
1014 type) and ZnO (*n*-type) was tested for CO gas sensing.¹¹² As
1015 in the case of tubular nanostructures,^{50,60,139} the thickness of
1016 the surface ZnO layer and the width of the depletion layer is
1017 vital to determine the responsivity. This core–shell structure
1018 depicted a low sensing detection limit than that of pristine
1019 ZnO and CuO nanofibers. By an appropriate choice of the
1020 thickness of the active layer/the top ZnO layer,^{60,139} a
1021 relatively higher sensitivity to the reducing gas may be
1022 obtained. The thickness of the shell modulates the depth of
1023 the depletion layer radially¹⁴² and can also influence the
1024 response time.⁵⁰ Nevertheless, the response of the ZnO based
1025 sensor to O₂ is inherently a slow process, where the oxygen can
1026 be adsorbed at the surface as well as at the defect sites,
1027 capturing an electron from the conduction band or defect site,
1028 respectively. Release of defect-bound-oxygen requires a free
1029 hole in the valence band which could be mediated by a photon
1030 of suitable energy. Indeed a sensor based on the spectral
1031 response will be discussed. By producing ZnO of higher optical
1032 quality or lesser oxygen vacancies through ALD, we may expect
1033 a faster response from the sensor. Despite a potential material

spectrum that ALD is capable of, only a limited number of
materials are tested for sensitivity by producing hierarchical
structures. There is a lot of scope in the context of Schottky
junctions where one can expect faster response and better
selectivity. The functionality of the earlier discussed gas-
sensors depends on the change in the electrical resistivity due
to the presence of the test gas molecule. Instead of electrical
means, interestingly, Viter et al.¹⁴³ investigated gas-detection
by monitoring the photoluminescence (PL) of ZnO-PAN
nanofibers. By monitoring the ratio of intensities from near
band edge emission (NBE) and deep level defect emissions
(DLE), the concentrations of the volatile organic compounds
are detected. Ethanol vapor (150 ppm) caused ~20% and 30%
for NBE and DLE intensity variations, respectively. This
sensitivity is indeed relatively low when compared to the
sensors based on variation in the conductivity. The sensitivity
of this particular sensor depends on the simultaneous intensity
of the two peaks in the PL spectrum, and this device may be
suitable for recognition of different volatile organic com-
pounds. Viter et al.¹⁴³ also showed that the PL signal is
stronger from ZnO-PAN nanofibers than that of ZnO on Si
substrate for the same quantity of the ZnO due to a large
improvement in the specific surface area of the nanofibers. A
spectrographic approach to gas sensors is known, and most of
the studies use electrical signal to sense a test gas. The easiness
in operation of gas sensors based on an electrical signal is
completely acknowledged. However, when the device response
is either low or slow, one might explore the possibility of a
spectroscopic approach for improved results. Notably, the
nanostructures act as waveguides increasing the detection
efficiency.

■ PHOTODETECTORS

UV response from wideband semiconductors, such as ZnO,
TiO₂, SnO₂, etc., has been extensively studied in their pristine
form as well as in heterointerfaces.^{53,64,110,144} For instance,
nanotubes of ZnO [ref 144] and TiO₂ [ref 64] were employed
as active materials in detectors, while the heterointerfaces
include BiVO₄-ZnO¹¹⁰ and SnO₂-ZnO.⁵³ Upon UV-illumina-
tion, the absorbed photons create electron–hole pairs. A
certain fraction of these electron–hole pairs may form excitons
followed by recombination which does not change the free
carrier concentration. However, on the other hand, the free
carriers, including dissociated excitons, transiently increase the
carrier concentration. The change in the free carrier
concentration increases the conductivity resulting in an
electrical signal. This is the basic detection mechanism of a
photon in a photodetector. Chaaya et al.¹⁴⁴ reported the
sensitive and stable UV sensing properties of ZnO nanotubes
and studied the effects of process parameters such as the
temperature of the substrate and electrospinning-time. Authors
reported that the sensor depicted promising stability over
multiple consecutive on–off cycles with a constant recovery
time. In this context, the mechanism of interaction between
surface defects and adsorbed gas molecules should be taken
into account when above band gap illumination of catalytically
active surfaces such as ZnO takes place, i.e., gas sensing
mechanism under UV illumination. TiO₂ and ZnO are vastly
employed UV-sensing elements, where the effects of UV light
on the defect chemistry of ZnO is rather complex.¹⁴⁵
Prolonged exposures to UV light affect surface and bulk
defects through catalytic activity of ZnO on the adsorbed
species and surface contaminants. Essentially, the electronic

1096 properties continuously change, which may not be the ideal
1097 scenario for photodetector applications, where change in the
1098 electrical conductivity is quantified against the photon
1099 intensity. Thus the calibration curve needs to be recalibrated.
1100 One can also think of passivating the thoroughly cleaned
1101 surface with insulating materials such as Al_2O_3 via ALD. Such
1102 coatings transmit the UV-light and hinder the surface
1103 adsorption of relatively larger molecular species. On the
1104 other hand, other wide band gap materials could also be
1105 considered.

1106 In the context of heterostructures, Hou et al.¹¹⁰ reported on
1107 the UV response of the $\text{BiVO}_4\text{-ZnO}$ heterostructure. The
1108 photocurrent density of $\sim 0.46 \text{ mA cm}^{-2}$ (at 1.23 V vs RHE)
1109 was observed under simulated sunlight irradiation, which is
1110 nearly 15.3 times higher than that of pristine BiVO_4
1111 nanoribbons. As discussed earlier, the built-in electric field
1112 (type-II) at the heterointerface enhanced the lifetime of the
1113 excited state carrier and separation rate of the excitons into free
1114 carriers. Note that the same strategy is applied on various other
1115 applications as discussed earlier. A further increase in the
1116 thickness of ZnO causes photocorrosion during the photo-
1117 chemical reaction. Hu et al.⁵³ has reported the construction of
1118 Ω -shaped hybrid (type-II) $\text{SnO}_2\text{-ZnO}$ UV detectors through
1119 the ALD of ZnO on SnO_2 nanofibers. The visibly transparent
1120 $\text{SnO}_2\text{-ZnO}$ heterostructure exhibited a relatively higher
1121 photoresponsivity ratio of 3.6×10^{-4} at 280 nm which is
1122 ~ 30 times higher than that of pristine SnO_2 nanofibers. Also
1123 wavelength selectivity of 2.0×10^3 (UV-vis rejection ratio,
1124 250–400 nm) is achieved by changing the direction of incident
1125 light. The Ω -shaped nanostructure increases the photon gain
1126 and trapping with faster electron-hole pair separation. IV
1127 curves, wavelength dependent responsivity, and band align-
1128 ment between SnO_2 and ZnO are shown in Figure 7f–h,
1129 respectively. The waveguide nature of the nanostructures is a
1130 fundamental capability that could be harnessed in photo-
1131 detectors, where there are a limited number of studies in this
1132 direction. At a specific wavelength, indeed, the wave guiding
1133 nature depends on the size of the nanostructures. Given the
1134 fact that it is difficult to obtain nanofibers of a uniform
1135 diameter with electrospinning, wave guiding at a specific
1136 wavelength would not be very easy. However, statistically,
1137 there are always some nanofibers which fall within the range of
1138 interest.

1139 ■ OUTLOOK AND CONCLUSION

1140 The potential to obtain hierarchical nanostructures from the
1141 combination of electrospinning and ALD are exemplified in
1142 this review. However, much larger scope is available for further
1143 developments where, postprocessing or other growth techni-
1144 ques (e.g., hydrothermal,⁴ solvothermal,¹²⁶) could be em-
1145 ployed on the nanostructures that were synthesized via
1146 combining electrospinning and ALD, e.g., metal-organic
1147 framework was grown on the nanofibers by the solvothermal
1148 technique.⁷⁰ However, these specific nanostructures were not
1149 subjected to any of the catalytic or other relevant applications.

1150 In the context of catalysis, degradation of the organic
1151 pollutant with inorganic catalyst is a smaller aspect of
1152 photocatalysis. The usage of photocatalyst in chemical
1153 reactions derived from this combination is still under
1154 exploitation given the fact that the catalysts could be produced
1155 in bulk quantities for industry. Also, the majority of the studies
1156 track the peak that is the characteristic of the organic pollutant.
1157 However, once the molecule fragments due to catalytic

1158 reactions, a complete degradation of the molecule is not
1159 traced. This will help us to understand the catalytically active
1160 site with reference to the adsorption configuration and
1161 molecular size. Furthermore, the BET surface area is
1162 extensively used to quantify the available surface area.
1163 However, all of these sites where N_2 adsorbs may not be
1164 available for the catalysis, where the molecule has to come to
1165 the site as close as 1 Å. Given the fact that the organic dye
1166 molecules are larger, a small molecule like N_2 may be adsorbed
1167 at several places which are not catalytically active. Hence,
1168 detailed and fundamental insights are still completely available
1169 for various catalysts and reactants. Studies in this direction will
1170 definitely increase the industrial applicability of these catalysts.

1171 Electrospinning and ALD could yield nanostructures of
1172 various materials which are not yet explored to their full
1173 potential toward solar cell applications. In principle, carefully
1174 processed nanofibers could form very good electron trans-
1175 porting channels, while the ALD can produce pinhole free
1176 conformal coatings of HBL layers. In fact, in energy storage
1177 applications, the electron transport through fibers is exploited.
1178 Notably, in general, the inorganic nanofibers consist of smaller
1179 grains, while the very nature of higher surface area to volume
1180 ratio increases the surface defects including grain boundaries.
1181 These grain boundaries and surface defects may be scattering/
1182 trapping centers for the charge carriers. This is beneficial for
1183 the catalysis; however, not for solar cells. Having said that,
1184 conformal coatings yielded from ALD could be studied for the
1185 passivation of such defect sites.⁵³ In the context of energy
1186 storage, a great deal of developments have taken place on the
1187 development of next generation anode materials for lithium
1188 and sulfur based batteries as well. On the other hand, in
1189 relation to gas sensors, relatively higher surface area to volume
1190 ratio yields higher gas sensitivity. The adsorption and
1191 desorption kinetics need to be considered in conjunction
1192 with the choice of material and the test gas, where extensive
1193 literature is available. Various hybrid structures have been
1194 studied toward photodetectors. Nevertheless, the capabilities
1195 of combination of ALD and electrospinning are under explored
1196 toward wavelength selective photodetectors, and we believe
1197 that there exists a lot of scope for the development of other
1198 novel hybrid nanostructures. For instance, a wide band gap
1199 semiconductor such as ZnO has been used as an active
1200 material in UV-detectors; however, suffering from lower
1201 response time which is generally attributed to the adsorp-
1202 tion/desorption of molecular oxygen due to UV exposure apart
1203 from various other effects as discussed by our group earlier.¹⁴⁶

1204 In this particular example, perhaps passivation schemes could
1205 be explored to enhance the performance of the device, where
1206 the conformal coating obtained from ALD might provide a
1207 solution.⁵³ There are various other semiconductors that could
1208 be produced through electrospinning; however, they are not
1209 explored for their wavelength-selective detection performance.

1210 Electrospun nanofibers act as a substrate and adsorb the
1211 ALD-precursor material. The quality of the interface is
1212 determined by the surface diffusion/infiltration of subsequent
1213 precursors. Indeed further experiments and analysis are
1214 required featuring high-resolution electron microscopy to
1215 image the immediate polymer/ALD coating interface. As an
1216 aside, notably, such an infiltration process (surface infiltrated
1217 synthesis) is actually being utilized to obtain composite
1218 organic/inorganic patterned films with potential applications
1219 in lithography-free nanofabrication. To conclude, ALD has
1220 become a common approach in catalysis for the deposition of

1221 metals and metal oxides on the supporting one-dimensional
1222 nanofibrous electrospun templates to allow their reusability
1223 and facile recycling from the products while enhancing their
1224 catalytic activity due to the chemical decoration of catalysts in
1225 an atomically controlled manner. The density and type of
1226 deposition of metal atoms can easily be adjusted by the
1227 changing the cycle number and process parameters. Depending
1228 on the type of metal or metal oxide used in the deposition, the
1229 catalytic applications of the resultant materials may show
1230 variations. While semiconductor metal oxides (e.g., ZnO and
1231 TiO₂) functional materials were commonly exploited for
1232 photocatalytic applications, the deposition of high catalytic
1233 noble metal atoms, such as Pd, Pt, and Ru, on electrospun
1234 fibers allows their use in nitroarene reduction and dehydrogen-
1235 ation reactions. Such metal deposited nanofibrous materials
1236 were also exploited for the electrochemical catalysis, including
1237 oxygen reduction/evolution reactions and water splitting. Since
1238 the catalytic metal atoms are chemically attached to the
1239 material surface, the resultant materials can be reused many
1240 times with similar catalytic activity with a further advantage of
1241 facile separation from the products. Overall, ALD is a unique
1242 and facile approach for the preparation of catalytic materials as
1243 mono or bimetallic nanoparticles and nanolayers on various
1244 electrospun materials, and therefore, their applications will find
1245 more application area in catalysis in the coming years. The
1246 potential of this combination could be further enhanced by
1247 preparing hierarchical structures through hydrothermal and
1248 other techniques. The combination of electrospinning and
1249 ALD has been vastly explored in energy storage applications,
1250 where lithium, sodium, and sulfur-based batteries were studied.
1251 Alternative anode-materials, such as MoS₂, Sn, etc. were
1252 studied with combinations of SnO₂, TiO₂, etc. The design of
1253 nanostructures is optimized such that the mechanical and
1254 structural integrity of the anode is retained accounting for
1255 volume changes during charge–discharge cycles, while not
1256 undermining the storage capacity of the battery. Also, the
1257 conventional electrodes based on carbon are also explored, and
1258 further improvements have been recorded through the
1259 deposition of metallic Sn, Ru nanoparticles. Heterostructures
1260 of ZnO, SnO₂, TiO₂, and CuO depicted unique surface
1261 functionalities and higher detection sensitivities toward ethanol
1262 vapor, O₂, NO₂, CO, NH₃, H₂, and others. Indeed, this gas
1263 sensitivity hinders the faster response when the same materials
1264 are used as photodetectors by forming a depletion layer at the
1265 surface. Under illumination, O₂ for instance desorbs from the
1266 surface which affects the photoluminescence of ZnO. By
1267 monitoring the photoluminescence, one can probe the
1268 concentration of gas by comparing the emissions across the
1269 near band edge and that of the defect level. Last, but not least,
1270 an amazing potential of electrospinning and ALD is seen with
1271 reference to the photodetectors. In this application, the
1272 heterostructures (example, BiVO₄-ZnO, SnO₂-ZnO) with a
1273 built-in electric field (due to band alignment) separates the
1274 photogenerated charge carriers enhancing the response.

1275 ■ AUTHOR INFORMATION

1276 Corresponding Authors

1277 **Sesha Vempati** – Department of Physics, Indian Institute of
1278 Technology Bhilai, Raipur 492015, India; orcid.org/0000-0002-0536-7827; Email: sesha@iitbhillai.ac.in
1279
1280 **Tamer Uyar** – Department of Fiber Science and Apparel Design,
1281 College of Human Ecology, Cornell University, Ithaca, New

York 14850, United States; orcid.org/0000-0002-3989-4481; Email: tu46@cornell.edu

1284 Authors

1285 **Kugalur Shanmugam Ranjith** – Department of Energy and
1286 Material Engineering, Dongguk University-Seoul, Seoul 04620,
1287 South Korea; orcid.org/0000-0003-3942-8672
1288 **Fuat Topuz** – Institute of Materials Science & Nanotechnology,
1289 UNAM-National Nanotechnology Research Center, Bilkent
1290 University, Ankara 06800, Turkey
1291 **Necmi Biyikli** – Electrical and Computer Engineering, University
1292 of Connecticut, Storrs, Connecticut 06269, United States

1293 Complete contact information is available at:
1294 <https://pubs.acs.org/10.1021/acsanm.0c01120>

1295 Notes

1296 The authors declare no competing financial interest.

1297 ■ REFERENCES

- 1298 (1) Ashfold, M. N. R.; Claeysens, F.; Fuge, G. M.; Henley, S. J. Pulsed Laser Ablation and Deposition of Thin Films. *Chem. Soc. Rev.* **2004**, *33*, 23–31. 1300
- 1301 (2) Crutchley, R. J. Chemical Vapor Deposition and Atomic Layer Deposition: Precursor Design and Application. *Coord. Chem. Rev.* **2013**, *257*, 3153–3384. 1303
- 1304 (3) Yan, Y.; Li, B.; Guo, W.; Pang, H.; Xue, H. Vanadium Based Materials as Electrode Materials for High Performance Supercapacitors. *J. Power Sources* **2016**, *329*, 148–169. 1306
- 1307 (4) Kayaci, F.; Vempati, S.; Ozgit-Akgun, C.; Biyikli, N.; Uyar, T. Enhanced Photocatalytic Activity of Homoassembled ZnO Nanostructures on Electrospun Polymeric Nanofibers: A Combination of Atomic Layer Deposition and Hydrothermal. *Appl. Catal., B* **2014**, *156–157*, 173–183. 1311
- 1312 (5) Doshi, J.; Reneker, D. H. Electrospinning Process and Applications of Electrospun Fibers. *J. Electrostat.* **1995**, *35*, 151–160. 1313
- 1314 (6) Ahvenniemi, E.; Akbashev, A. R.; Ali, S.; Bechelany, M.; Berdova, M.; Boyadjiev, S.; Cameron, D. C.; Chen, R.; Chubarov, M.; Cremers, V.; Devi, A.; Drozd, V.; Elnikova, L.; Gottardi, G.; Grigoras, K.; Hausmann, D. M.; Hwang, C. S.; Jen, S.-H.; Kallio, T.; Kanervo, J.; Khmelnskiy, I.; Kim, D. H.; Klibanov, L.; Koshtyal, Y.; Krause, A. O. I.; Kuhs, J.; Karkkanen, I.; Kaariainen, M.-L.; Kaariainen, T.; Lamagna, L.; Łapicki, A. A.; Leskela, M.; Lipsanen, H.; Lyytinen, J.; Malkov, A.; Malygin, A.; Mennad, A.; Militzer, C.; Molariu, J.; Norek, M. I.; Ozgit-Akgun, C.; Panov, M.; Pedersen, H.; Piallat, F.; Popov, G.; Puurunen, R. L.; Rampelberg, G.; Ras, R. H. A.; Rauwel, E.; Roozeboom, F.; Sajavaara, T.; Salami, H.; Savin, H.; Schneider, N.; Seidel, T. E.; Sundqvist, J.; Suyatin, D. B.; Torndahl, T.; van Ommen, J. R.; Wiemer, C.; Ylivaara, O. M. E.; Yurkevich, O. Review Article: Recommended Reading List of Early Publications on Atomic Layer Deposition—Outcome of the “Virtual Project on the History of Ald. *J. Vac. Sci. Technol., A* **2017**, *35*, 010801. 1329
- 1330 (7) Ritala, M.; Leskelä, M. *Atomic Layer Deposition in Handbook of Thin Film Materials*; Nalwa, H. S., Ed.; Academic: San Diego, CA, 2002; Vol. 1, pp 103–159. 1332
- 1333 (8) Puurunen, R. L. Surface Chemistry of Atomic Layer Deposition: A Case Study for the Trimethylaluminum/Water Process. *J. Appl. Phys.* **2005**, *97*, 121301. 1335
- 1336 (9) George, S. M. Atomic Layer Deposition: An Overview. *Chem. Rev.* **2010**, *110*, 111. 1337
- 1338 (10) Parsons, G. N.; Elam, J. W.; George, S. M.; Haukka, S.; Jeon, H.; Kessels, W. M. M.; Leskela, M.; Poedt, P.; Ritala, M.; Rossnagel, S. M. History of Atomic Layer Deposition and Its Relationship with the American Vacuum Society. *J. Vac. Sci. Technol., A* **2013**, *31*, 050818. 1342
- 1343 (11) Vempati, S.; Shetty, A.; Dawson, P.; Nanda, K.; Krupanidhi, S. Solution-Based Synthesis of Cobalt-Doped ZnO Thin Films. *Thin Solid Films* **2012**, *524*, 137–143. 1345

- 1346 (12) Vempati, S.; Shetty, A.; Dawson, P.; Nanda, K.; Krupanidhi, S.
1347 Cobalt-Doped Zn Nanowires on Quartz: Synthesis by Simple
1348 Chemical Method and Characterization. *J. Cryst. Growth* **2012**, *343*,
1349 7–12.
- 1350 (13) Taylor, G. I. Electrically Driven Jets. *Proc. Roy. Soc. Lond A*
1351 **1969**, *313*, 453–475.
- 1352 (14) Celebioglu, A.; Uyar, T. Cyclodextrin Nanofibers by Electro-
1353 spinning. *Chem. Commun.* **2010**, *46*, 6903–6905.
- 1354 (15) Mackus, A. J. M.; Bol, A. A.; Kessels, W. M. M. The Use of
1355 Atomic Layer Deposition in Advanced Nanopatterning. *Nanoscale*
1356 **2014**, *6*, 10941–10960.
- 1357 (16) Zheng, Y. B.; Juluri, B. K.; Mao, X.; Walker, T. R.; Huang, T. J.
1358 Systematic Investigation of Localized Surface Plasmon Resonance of
1359 Long-Range Ordered Au Nanodisk Arrays. *J. Appl. Phys.* **2008**, *103*,
1360 014308.
- 1361 (17) Xie, M.; Sun, X.; Zhou, C.; Cavanagh, A. S.; Sun, H.; Hu, T.;
1362 Wang, G.; Lian, J.; George, S. M. Amorphous Ultrathin TiO₂ Atomic
1363 Layer Deposition Films on Carbon Nanotubes as Anodes for Lithium
1364 Ion Batteries. *J. Electrochem. Soc.* **2015**, *162*, A974–A981.
- 1365 (18) Jung, S.-K.; Gwon, H.; Hong, J.; Park, K.-Y.; Seo, D.-H.; Kim,
1366 H.; Hyun, J.; Yang, W.; Kang, K. Understanding the Degradation
1367 Mechanisms of LiNi_{0.5}Co_{0.2}Mn_{0.3}O₂ Cathode Material in Lithium Ion
1368 Batteries. *Adv. Energy Mater.* **2014**, *4*, 1300787.
- 1369 (19) van-Delft, J. A.; Garcia-Alonso, D.; Kessels, W. M. M. Atomic
1370 Layer Deposition for Photovoltaics: Applications and Prospects for
1371 Solar Cell Manufacturing. *Semicond. Sci. Technol.* **2012**, *27*, 074002.
- 1372 (20) Schmidt, J.; Merkle, A.; Brendel, R.; Hoex, B.; de Sanden, M. C.
1373 M. v.; Kessels, W. M. M. Surface Passivation of High-Efficiency
1374 Silicon Solar Cells by Atomic-Layer-Deposited Al₂O₃. *Prog. Photo-*
1375 *voltaics* **2008**, *16*, 461.
- 1376 (21) Richter, A.; Benick, J.; Hermle, M.; Glunz, S. W. Excellent
1377 Silicon Surface Passivation with 5 Å Thin Al₂O₃ Layers: Influence
1378 of Different Thermal Post-Deposition Treatments. *Phys. Status Solidi*
1379 *RRL* **2011**, *5*, 202.
- 1380 (22) O'Neill, B. J.; Jackson, D. H. K.; Lee, J.; Canlas, C.; Stair, P. C.;
1381 Marshall, C. L.; Elam, J. W.; Kuech, T. F.; Dumesic, J. A.; Huber, G.
1382 W. Catalyst Design with Atomic Layer Deposition. *ACS Catal.* **2015**,
1383 *5*, 1804–1825.
- 1384 (23) Lu, J.; Elam, J. W.; Stair, P. C. Synthesis and Stabilization of
1385 Supported Metal Catalysts by Atomic Layer Deposition. *Acc. Chem.*
1386 *Res.* **2013**, *46*, 1806–1815.
- 1387 (24) Khalily, M. A.; Eren, H.; Akbayrak, S.; Susapto, H. H.; Biyikli,
1388 N.; Özkar, S.; Guler, M. O. Facile Synthesis of Three-Dimensional Pt-
1389 TiO₂ Nano-Networks: A Highly Active Catalyst for the Hydrolytic
1390 Dehydrogenation of Ammonia-Borane. *Angew. Chem., Int. Ed.* **2016**,
1391 *55*, 12257.
- 1392 (25) Kim, B. J.; Kim, D. H.; Lee, Y.-Y.; Shin, H.-W.; Han, G. S.;
1393 Hong, J. S.; Mahmood, K.; Ahn, T. K.; Joo, Y.-C.; Hong, K. S.; Park,
1394 N.-G.; Lee, S.; Jung, H. S. Highly Efficient and Bending Durable
1395 Perovskite Solar Cells: Toward a Wearable Power Source. *Energy*
1396 *Environ. Sci.* **2015**, *8*, 916.
- 1397 (26) Sheng, J.; Han, K.-L.; Hong, T. H.; Choi, W.-H.; Park, J.-S.
1398 Review of Recent Progresses on Flexible Oxide Semiconductor Thin
1399 Film Transistors Based on Atomic Layer Deposition Processes. *J.*
1400 *Semicond.* **2018**, *39*, 011008.
- 1401 (27) Jung, J.-W.; Lee, C.-L.; Yu, S.; Kim, I.-D. Electrospun
1402 Nanofibers as a Platform for Advanced Secondary Batteries: A
1403 Comprehensive Review. *J. Mater. Chem. A* **2016**, *4*, 703–750.
- 1404 (28) Thomas, M.; Rajiv, S. Dye-Sensitized Solar Cells Based on an
1405 Electrospun Polymer Nanocomposite Membrane as Electrolyte. *New*
1406 *J. Chem.* **2019**, *43*, 4444–4454.
- 1407 (29) Pan, S.; Wang, Y.; Li, M.; Huang, G.; Mei, Y. *Method for*
1408 *Preparing Photoanode of Dye-Sensitized Solar Cell*. Chinese Patent
1409 CN102832051A, 2012.
- 1410 (30) Qin, X.; Subianto, S. *Electrospun Nanofibers for Filtration*
1411 *Applications*; Woodhead Publishing Series in Textiles, 2017.
- 1412 (31) Mirjalili, M.; Zohoori, S. Review for Application of Electro-
1413 spinning and Electrospun Nanofibers Technology in Textile Industry.
1414 *J. Nanostruct. Chem.* **2016**, *6*, 207–213.
- (32) Uyar, T.; Kny, E. *Electrospun Materials for Tissue Engineering*
1415 *and Biomedical Applications: Research, Design and Commercialization*;
1416 Woodhead Publishing, 2017.
- (33) Torres-Martinez, E. J.; Cornejo Bravo, J. M.; Serrano Medina,
1418 A.; Perez Gonzalez, G. L.; Villarreal Gomez, L. J. A Summary of
1419 Electrospun Nanofibers as Drug Delivery System: Drugs Loaded and
1420 Biopolymers Used as Matrices. *Curr. Drug Delivery* **2018**, *15*, 1360–
1421 1374.
- (34) Thavasi, V.; Singh, G.; Ramakrishna, S. Electrospun Nanofibers
1423 in Energy and Environmental Applications. *Energy Environ. Sci.* **2008**,
1424 *1*, 205–221.
- (35) Arslan, O.; Topuz, F.; Eren, H.; Biyikli, N.; Uyar, T. Pd
1426 Nanocube Decoration onto Flexible Nanofibrous Mats of Core-Shell
1427 Polymer-Zn Nanofibers for Visible Light Photocatalysis. *New J.*
1428 *Chem.* **2017**, *41*, 4145–4156.
- (36) Li, J.; Chen, X.; Xu, W.; Nam, C.-Y.; Shi, Y. TiO₂ Nanofiber
1430 Solid-State Dye Sensitized Solar Cells with Thin TiO₂ Hole Blocking
1431 Layer Prepared by Atomic Layer Deposition. *Thin Solid Films* **2013**,
1432 *536*, 275–279.
- (37) Ryu, W.-H.; Jung, J.-W.; Park, K.; Kim, S.-J.; Kim, I.-D. Vine-
1434 Like MoS₂ Anode Materials Self-Assembled from 1-D Nanofibers for
1435 High Capacity Sodium Rechargeable Batteries. *Nanoscale* **2014**, *6*,
1436 10975–10981.
- (38) Mao, M.; Yan, F.; Cui, C.; Ma, J.; Zhang, M.; Wang, T.; Wang,
1438 C. Pipe-Wire TiO₂-Sn@Carbon Nanofibers Paper Anodes for
1439 Lithium and Sodium Ion Batteries. *Nano Lett.* **2017**, *17*, 3830–3836.
- (39) Wang, X.; Fan, L.; Gong, D.; Zhu, J.; Zhang, Q.; Lu, B. Core-
1441 Shell Ge@Graphene@TiO₂ Nanofibers as a High-Capacity and
1442 Cycle-Stable Anode for Lithium and Sodium Ion Battery. *Adv. Funct.*
1443 *Mater.* **2016**, *26*, 1104–1111.
- (40) Yang, J.; Mi, H.; Luo, S.; Li, Y.; Zhang, P.; Deng, L.; Sun, L.;
1445 Ren, X. Atomic Layer Deposition of TiO₂ on Nitrogen-Doped Carbon
1446 Nanofibers Supported Ru Nanoparticles for Flexible Li-O₂ Battery: A
1447 Combined Dft and Experimental Study. *J. Power Sources* **2017**, *368*,
1448 88–96.
- (41) Zhu, Y.; Fan, X.; Suo, L.; Luo, C.; Gao, T.; Wang, C.
1450 Electrospun FeS₂@Carbon Fiber Electrode as a High Energy Density
1451 Cathode for Rechargeable Lithium Batteries. *ACS Nano* **2016**, *10*,
1452 1529–1538.
- (42) Shen, X.; Li, C.; Shi, C.; Yang, C.; Deng, L.; Zhang, W.; Peng,
1454 L.; Dai, J.; Wu, D.; Zhang, P.; Zhao, J. Core-Shell Structured Ceramic
1455 Nonwoven Separators by Atomic Layer Deposition for Safe Lithium-
1456 Ion Batteries. *Appl. Surf. Sci.* **2018**, *441*, 165–173.
- (43) Ma, D.; Li, Y.; Yang, J.; Mi, H.; Luo, S.; Deng, L.; Yan, C.; Rauf,
1458 M.; Zhang, P.; Sun, X.; Ren, X.; Li, J.; Zhang, H. New Strategy for
1459 Polysulfide Protection Based on Atomic Layer Deposition of TiO₂
1460 onto Ferroelectric-Encapsulated Cathode: Toward Ultra Stable Free-
1461 Standing Room Temperature Sodium-Sulfur Batteries. *Adv. Funct.*
1462 *Mater.* **2018**, *28*, 1705537.
- (44) Zhu, J.; Wang, T.; Fan, F.; Mei, L.; Lu, B. Atomic-Scale Control
1464 of Silicon Expansion Space as Ultrastable Battery Anodes. *ACS Nano*
1465 **2016**, *10*, 8243–8251.
- (45) Kayaci, F.; Vempati, S.; Ozgit-Akgun, C.; Donmez, I.; Biyikli,
1467 N.; Uyar, T. Transformation of Polymer-Zn Core-Shell Nanofibers
1468 into Zn Hollow Nanofibers: Intrinsic Defect Reorganization in Zn
1469 and Its Influence on the Photocatalysis. *Appl. Catal., B* **2015**, *176*–
1470 *177*, 646–653.
- (46) Kayaci, F.; Vempati, S.; Ozgit-Akgun, C.; Donmez, I.; Biyikli,
1472 N.; Uyar, T. Selective Isolation of the Electron or Hole in
1473 Photocatalysis: ZnO-TiO₂ and TiO₂-ZnO Core-Shell Structured
1474 Heterojunction Nanofibers Via Electrospinning and Atomic Layer
1475 Deposition. *Nanoscale* **2014**, *6*, 5735–5745.
- (47) Lopez de Dicastillo, C.; Patino, C.; Galotto, M. J.; Palma, J. L.;
1477 Alburquenque, D.; Escrig, J. Novel Antimicrobial Titanium Dioxide
1478 Nanotubes Obtained through a Combination of Atomic Layer
1479 Deposition and Electrospinning Technologies. *Nanomaterials* **2018**,
1480 *8*, 128.
- (48) Weber, M.; Iatsunskiy, I.; Coy, E.; Miele, P.; Cornu, D.;
1482 Bechelany, M. Novel and Facile Route for the Synthesis of Tunable
1483

- 1484 Boron Nitride Nanotubes Combining Atomic Layer Deposition and
1485 Annealing Processes for Water Purification. *Adv. Mater. Interfaces*
1486 **2018**, *5*, 1800056.
- 1487 (49) Hao, W.; Marichy, C.; Brioude, A. Promising Properties of Ald
1488 Boron Nitride Nanotube Mats for Water Purification. *Environ. Sci.:*
1489 *Nano* **2017**, *4*, 2311–2320.
- 1490 (50) Boyadjiev, S. I.; Keri, O.; Bardos, P.; Firkala, T.; Gaber, F.;
1491 Nagy, Z. K.; Baji, Z.; Takacs, M.; Szilagy, I. M. Tio₂/Zno and Zno/
1492 Tio₂ Core/Shell Nanofibers Prepared by Electrospinning and Atomic
1493 Layer Deposition for Photocatalysis and Gas Sensing. *Appl. Surf. Sci.*
1494 **2017**, *424*, 190–197.
- 1495 (51) Park, J. Y.; Choi, S.-W.; Lee, J.-W.; Lee, C.; Kim, S. S. Synthesis
1496 and Gas Sensing Properties of Tio₂-Zno Core-Shell Nanofibers. *J.*
1497 *Am. Ceram. Soc.* **2009**, *92*, 2551–2554.
- 1498 (52) Viter, R.; Iatsunskiy, I.; Fedorenko, V.; Tumenas, S.; Balevicius,
1499 Z.; Ramanavicius, A.; Balme, S.; Kempinski, M.; Nowaczyk, G.; Jurga,
1500 S.; Bechelany, M. Enhancement of Electronic and Optical Properties
1501 of Zno/Al₂O₃ Nanolaminate Coated Electrospun Nanofibers. *J. Phys.*
1502 *Chem. C* **2016**, *120*, 5124–5132.
- 1503 (53) Hu, M.; Teng, F.; Chen, H.; Jiang, M.; Gu, Y.; Lu, H.; Hu, L.;
1504 Fang, X. Novel Ω-Shaped Core-Shell Photodetector with High
1505 Ultraviolet Selectivity and Enhanced Responsivity. *Adv. Funct. Mater.*
1506 **2017**, *27*, 1704477.
- 1507 (54) Ozgit-Akgun, C.; Kayaci, F.; Vempati, S.; Haider, A.;
1508 Celebioglu, A.; Goldenberg, E.; Kizir, S.; Uyar, T.; Biyikli, N.
1509 Fabrication of Flexible Polymer-Gan Core-Shell Nanofibers by the
1510 Combination of Electrospinning and Hollow Cathode Plasma-
1511 Assisted Atomic Layer Deposition. *J. Mater. Chem. C* **2015**, *3*,
1512 5199–5206.
- 1513 (55) Haider, A.; Ozgit-Akgun, C.; Kayaci, F.; Okyay, A. K.; Uyar, T.;
1514 Biyikli, N. Fabrication of Aln/Bn Bishell Hollow Nanofibers by
1515 Electrospinning and Atomic Layer Deposition. *APL Mater.* **2014**, *2*,
1516 096109.
- 1517 (56) Jeun, J.-H.; Park, K.-Y.; Kim, D.-H.; Kim, W.-S.; Kim, H.-C.;
1518 Lee, B.-S.; Kim, H.; Yu, W.-R.; Kang, K.; Hong, S.-H. Sno₂@Tio₂
1519 Double-Shell Nanotubes for a Lithium Ion Battery Anode with
1520 Excellent High Rate Cyclability. *Nanoscale* **2013**, *5*, 8480–8483.
- 1521 (57) Katoch, A.; Kim, J.-H.; Kim, S. S. Tio₂/Zno Inner/Outer
1522 Double-Layer Hollow Fibers for Improved Detection of Reducing
1523 Gases. *ACS Appl. Mater. Interfaces* **2014**, *6*, 21494–21499.
- 1524 (58) Donmez, I.; Kayaci, F.; Ozgit-Akgun, C.; Uyar, T.; Biyikli, N.
1525 Fabrication of Hafnia Hollow Nanofibers by Atomic Layer Deposition
1526 Using Electrospun Nanofiber Templates. *J. Alloys Compd.* **2013**, *559*,
1527 146–151.
- 1528 (59) Ozgit-Akgun, C.; Kayaci, F.; Donmez, I.; Uyar, T.; Biyikli, N.
1529 Template-Based Synthesis of Aln Hollow Nanofibers Via Plasma-
1530 Enhanced Atomic Layer Deposition. In *Nanotech Conference & Expo*
1531 **2012: An Interdisciplinary Integrative Forum on Nanotechnology,
1532 *Microtechnology, Biotechnology and Cleantechology*, Santa Clara, CA,
1533 June 18–21, 2012, CRC Press, 2012; pp 675–678.**
- 1534 (60) Katoch, A.; Choi, S.-W.; Sub Kim, S. Effect of the Wall
1535 Thickness on the Gas-Sensing Properties of Zno Hollow Fibers.
1536 *Nanotechnology* **2014**, *25*, 455504.
- 1537 (61) Park, J. Y.; Choi, S.-W.; Kim, S. S. A Synthesis and Sensing
1538 Application of Hollow Zno Nanofibers with Uniform Wall
1539 Thicknesses Grown Using Polymer Templates. *Nanotechnology*
1540 **2010**, *21*, 475601.
- 1541 (62) Heikkilae, P.; Hirvikorpi, T.; Hilden, H.; Sievaenen, J.;
1542 Hyvaerinen, L.; Harlin, A.; Vaehae-Nissi, M. High Surface Area
1543 Nanostructured Tubes Prepared by Dissolution of Ald-Coated
1544 Electrospun Fibers. *J. Mater. Sci.* **2012**, *47*, 3607–3612.
- 1545 (63) Saquing, C. D.; Peng, Q.; Parsons, G. N.; Khan, S. A. Metal
1546 Nanoparticle-Loaded Al₂O₃ Microtubes by Atomic Layer Deposition
1547 on Nanofiber Composite Templates. In *235th ACS Spring National*
1548 *Meeting*, New Orleans, LA, April 6–10, 2008, American Chemical
1549 Society, 2008; pp PHYS-491.
- 1550 (64) Choi, S.-W.; Park, J. Y.; Lee, C.; Lee, J. G.; Kim, S. S. Synthesis
1551 of Highly Crystalline Hollow Tio₂ Fibers Using Atomic Layer
Deposition on Polymer Templates. *J. Am. Ceram. Soc.* **2011**, *94*, 1552
1974–1977.
- (65) Kim, W.-S.; Lee, B.-S.; Kim, D.-H.; Kim, H.-C.; Yu, W.-R.;
Hong, S.-H. Sno₂ Nanotubes Fabricated Using Electrospinning and
Atomic Layer Deposition and Their Gas Sensing Performance. *1555*
Nanotechnology **2010**, *21*, 245605. 1557
- (66) Pereira, A.; Escrig, J.; Palma, J. L.; de Dicastillo, C. L.; Patino,
C.; Galotto, M. J. Magnetic Nanotubes Obtained from Atomic Layer
Deposition Coated Electrospun Nanofibers. *J. Vac. Sci. Technol., B:*
Nanotechnol. Microelectron.: Mater., Process., Meas., Phenom. **2018**, *36*,
061803. 1562
- (67) Liang, Z.; Hou, H.; Song, K.; Zhang, K.; Fang, Z.; Gao, F.;
Wang, L.; Chen, D.; Yang, W.; Zeng, H. Boosting the Photo-
electrochemical Activities of All-Inorganic Perovskite Sr₂Co₂ Nano-
fibers by Engineering Homo/Hetero Junctions. *J. Mater. Chem. A* **2018**, *6*,
17530–17539. 1567
- (68) Celebioglu, A.; Ranjith, K. S.; Eren, H.; Biyikli, N.; Uyar, T.
Surface Decoration of Pt Nanoparticles Via Ald with Tio₂ Protective
Layer on Polymeric Nanofibers as Flexible and Reusable Heteroge-
neous Nanocatalysts. *Sci. Rep.* **2017**, *7*, 13401. 1571
- (69) Di Mauro, A.; Fragala, M. E.; Privitera, V.; Impellizzeri, G. Zno
for Application in Photocatalysis: From Thin Films to Nanostruc-
tures. *Mater. Sci. Semicond. Process.* **2017**, *69*, 44–51. 1574
- (70) Bechelany, M.; Drobek, M.; Vallicari, C.; Abou Chaaya, A.;
Julbe, A.; Miele, P. Highly Crystalline Mof-Based Materials Grown on
Electrospun Nanofibers. *Nanoscale* **2015**, *7*, 5794–5802. 1577
- (71) Sundaray, B.; Subramanian, V.; Natarajan, T. S.; Xiang, R.-Z.;
Chang, C.-C.; Fann, W.-S. Electrospinning of Continuous Aligned
Polymer Fibers. *Appl. Phys. Lett.* **2004**, *84*, 1222. 1580
- (72) Celebioglu, A.; Vempati, S.; Ozgit-Akgun, C.; Biyikli, N.; Uyar,
T. Water-Soluble Non-Polymeric Electrospun Cyclodextrin Nanofiber
Template for the Synthesis of Metal Oxide Tubes by Atomic Layer
Deposition. *RSC Adv.* **2014**, *4*, 61698–61705. 1584
- (73) Pavan Kumar, V. S.; Jagadeesh Babu, V.; Raghuraman, G. K.;
Dhamodharan, R.; Natarajan, T. S. Electrospinning Can Be with
Composites Not Just Pure Polymers. Giant Magnetoresistance of
-Polymethylmethacrylate Nanocomposite Aligned Fibers Via Electro-
spinning. *J. Appl. Phys.* **2007**, *101*, 114317. 1589
- (74) Persano, L.; Camposo, A.; Tekmen, C.; Pisignano, D.
Industrial Upscaling of Electrospinning and Applications of Polymer
Nanofibers: A Review. *Macromol. Mater. Eng.* **2013**, *298*, S04–S20. 1592
- (75) Simons, H. L. *Process and Apparatus for Producing Patterned*
Non-Woven Fabrics. U.S. Patent 3,280,229. 1966. 1594
- (76) How, T. V. *Synthetic Vascular Grafts and Methods of*
Manufacturing Such Grafts, Us Patent Number No. US4552707, 1596
1985. 1597
- (77) Berry, J. P. *Method and Apparatus for Manufacturing*
Electrostatically Spun Structure. U.S. Patent 5,024,789, 1991. 1599
- (78) Kijenska, E.; Swieszkowski, W. *Electrospun Materials for Tissue*
Engineering and Biomedical Applications: Research, Design and
Commercialization; Woodhead Publishing, 2017. 1602
- (79) Topuz, F.; Abdulhamid, M. A.; Nunes, S. P.; Szekely, G.
Hierarchically Porous Electrospun Nanofibrous Mats Produced from
Intrinsically Microporous Fluorinated Polyimide for the Removal of
Oils and Non-Polar Solvents. *Environ. Sci.: Nano* **2020**, 1606
DOI: 10.1039/DOEN0084A. 1607
- (80) Topuz, F.; Uyar, T. Antioxidant, Antibacterial and Antifungal
Electrospun Nanofibers for Food Packaging Applications. *Food Res.*
Int. **2020**, *130*, 108927. 1610
- (81) Vempati, S.; Natarajan, T. Flexible Polymer Microtubes and
Microchannels Via Electrospinning. *Mater. Lett.* **2011**, *65*, 3493–
3495. 1613
- (82) Patil, B.; Satilmis, B.; Khalily, M. A.; Uyar, T. ALD of Ni(OOH)/
Ni(OH)₂ on Pim-1 Based Free-Standing Flexible Binder-Free
Electrospun N-Doped Carbon Nanofibers: Nanocatalyst for Electro-
chemical Water Splitting in Alkaline Medium. *ChemSusChem* **2019**,
12, 1469–1477. 1618

- 1619 (83) Srivastava, Y.; Marquez, M.; Thorsen, T. Microfluidic
1620 Electrospinning of Biphasic Nanofibers with Janus Morphology.
1621 *Biomicrofluidics* **2009**, *3*, 012801.
- 1622 (84) Budd, P. M.; Ghanem, B. S.; Makhseed, S.; McKeown, N. B.;
1623 Msayib, K. J.; Tattershall, C. E. Polymers of Intrinsic Microporosity
1624 (Pims): Robust, Solution-Processable, Organic Nanoporous Materi-
1625 als. *Chem. Commun.* **2004**, *4*, 230–231.
- 1626 (85) <https://www.inovenso.com>.
- 1627 (86) <http://bioinicia.com/>.
- 1628 (87) <http://www.yflow.com/>.
- 1629 (88) <http://www.electrospinning.co.uk>.
- 1630 (89) <http://www.imetechnologies.com>.
- 1631 (90) <https://www.spraybase.com/>.
- 1632 (91) <http://www.linariobiomedical.com/index.php/electrospinning>.
- 1633 (92) <https://www.elmarco.com/>.
- 1634 (93) <https://www.4spin.info/>.
- 1635 (94) <https://spingenix.com/>.
- 1636 (95) <http://www.espintechologies.com/>.
- 1637 (96) <http://www.nanofibersolutions.com>.
- 1638 (97) www.holmarc.com.
- 1639 (98) <https://www.electro-spinning.com/>.
- 1640 (99) <https://www.mecc-nano.com/>.
- 1641 (100) <http://www.sncfibers.com/>.
- 1642 (101) <http://revolutionfibres.com/>.
- 1643 (102) <https://www.electro-spinning.com/electrospinning-spinneret.html>.
- 1644 (103) Balogh, A.; Farkas, B.; Verreck, G.; Mensch, J.; Borbás, E.;
1645 Nagy, B.; Marosi, G.; Nagy, Z. K. Ac and Dc Electrospinning of
1646 Hydroxypropylmethylcellulose with Polyethylene Oxides as Sec-
1647 ondary Polymer for Improved Drug Dissolution. *Int. J. Pharm.* **2016**,
1648 *505*, 159–166.
- 1650 (104) Knoops, H. C. M.; Faraz, T.; Arts, K.; Kessels, W. M. M.
1651 Status and Prospects of Plasma-Assisted Atomic Layer Deposition. *J.*
1652 *Vac. Sci. Technol., A* **2019**, *37*, 030902.
- 1653 (105) Mohammad, A.; Shukla, D.; Ilhom, S.; Willis, B.; Johs, B.;
1654 Okyay, A. K.; Biyikli, N. Real-Time in Situ Ellipsometric Monitoring
1655 of Aluminum Nitride Film Growth Via Hollow-Cathode Plasma-
1656 Assisted Atomic Layer Deposition. *J. Vac. Sci. Technol., A* **2019**, *37*,
1657 020927.
- 1658 (106) Ozgit-Akgun, C.; Kayaci, F.; Donmez, I.; Uyar, T.; Biyikli, N.
1659 Template-Based Synthesis of Aluminum Nitride Hollow Nanofibers
1660 Via Plasma-Enhanced Atomic Layer Deposition. *J. Am. Ceram. Soc.*
1661 **2013**, *96*, 916.
- 1662 (107) Vempati, S.; Kayaci-Senirmak, F.; Ozgit-Akgun, C.; Biyikli, N.;
1663 Uyar, T. Amorphous to Tetragonal Zirconia Nanostructures and
1664 Evolution of Valence and Core Regions. *J. Phys. Chem. C* **2015**, *119*,
1665 23268–23273.
- 1666 (108) Nasr, M.; Viter, R.; Eid, C.; Warmont, F.; Habchi, R.; Miele,
1667 P.; Bechelany, M. Synthesis of Novel ZnO/ZnAl₂O₄ Multi Co-Centric
1668 Nanotubes and Their Long-Term Stability in Photocatalytic
1669 Application. *RSC Adv.* **2016**, *6*, 103692–103699.
- 1670 (109) Kayaci, F.; Ozgit-Akgun, C.; Biyikli, N.; Uyar, T. Surface-
1671 Decorated ZnO Nanoparticles and ZnO Nanocoating on Electrospun
1672 Polymeric Nanofibers by Atomic Layer Deposition for Flexible
1673 Photocatalytic Nanofibrous Membranes. *RSC Adv.* **2013**, *3*, 6817–
1674 6820.
- 1675 (110) Hou, H.; Liu, H.; Gao, F.; Shang, M.; Wang, L.; Xu, L.; Wong,
1676 W.-Y.; Yang, W. Packaging BiVO₄ Nanoparticles in ZnO Microbelts for
1677 Efficient Photoelectrochemical Hydrogen Production. *Electrochim.*
1678 *Acta* **2018**, *283*, 497–508.
- 1679 (111) Lee, B.-S.; Kim, W.-S.; Kim, D.-H.; Kim, H.-C.; Hong, S.-H.;
1680 Yu, W.-R. Fabrication of SnO₂ Nanotube Microarray and Its Gas
1681 Sensing Behavior. *Smart Mater. Struct.* **2011**, *20*, 105019.
- 1682 (112) Katoch, A.; Choi, S.-W.; Sun, G.-J.; Kim, H. W.; Kim, S. S.
1683 Mechanism and Prominent Enhancement of Sensing Ability to
1684 Reducing Gases in P/N Core-Shell Nanofiber. *Nanotechnology* **2014**,
1685 *25*, 175501.
- 1686 (113) Szilágyi, I. M.; Santala, E.; Heikkilä, M.; Pore, V.; Kemell, M.;
1687 Nikitin, T.; Teucher, G.; Firkala, T.; Khriachtchev, L.; Räsänen, M.;
1688 Ritala, M.; Leskelä, M. Photocatalytic Properties of WO₃/TiO₂ Core/
1689 Shell Nanofibers Prepared by Electrospinning and Atomic Layer
1690 Deposition. *Chem. Vap. Deposition* **2013**, *19*, 149–155.
- 1691 (114) Jean, J.-H.; Kwak, H.; Kim, W.-S.; Kim, H.-C.; Park, K.-Y.;
1692 Kim, H.; Yang, H.-S.; Yu, W.-R.; Kang, K.; Hong, S.-H. Tio₂@SnO₂@
1693 Tio₂ Triple-Shell Nanotube Anode for High-Performance Lithium-
1694 Ion Batteries. *J. Solid State Electrochem.* **2017**, *21*, 2365–2371.
- 1695 (115) Mills, A.; Le Hunte, S. An Overview of Semiconductor
1696 Photocatalysis. *J. Photochem. Photobiol., A* **1997**, *108*, 1–35.
- 1697 (116) Fox, M. A.; Dulay, M. T. Heterogeneous Photocatalysis.
1698 *Chem. Rev.* **1993**, *93*, 341–357.
- 1699 (117) Lang, X.; Chen, X.; Zhao, J. Heterogeneous Visible Light
1700 Photocatalysis for Selective Organic Transformations. *Chem. Soc. Rev.*
1701 **2014**, *43*, 473–486.
- 1702 (118) Khalily, M. A.; Yurderi, M.; Haider, A.; Bulut, A.; Patil, B.;
1703 Zahmakiran, M.; Uyar, T. Atomic Layer Deposition of Ruthenium
1704 Nanoparticles on Electrospun Carbon Nanofibers: A Highly Efficient
1705 Nanocatalyst for the Hydrolytic Dehydrogenation of Methylamine
1706 Borane. *ACS Appl. Mater. Interfaces* **2018**, *10*, 26162–26169.
- 1707 (119) Kayaci, F.; Ozgit-Akgun, C.; Donmez, I.; Biyikli, N.; Uyar, T.
1708 Polymer-Inorganic Core-Shell Nanofibers by Electrospinning and
1709 Atomic Layer Deposition: Flexible Nylon-ZnO Core-Shell Nanofiber
1710 Mats and Their Photocatalytic Activity. *ACS Appl. Mater. Interfaces*
1711 **2012**, *4*, 6185–6194.
- 1712 (120) Di Mauro, A.; Fragalà, M. E.; Privitera, V.; Impellizzeri, G.
1713 ZnO for Application in Photocatalysis: From Thin Films to
1714 Nanostructures. *Mater. Sci. Semicond. Process.* **2017**, *69*, 44–51.
- 1715 (121) Nasr, M.; Viter, R.; Eid, C.; Habchi, R.; Miele, P.; Bechelany,
1716 M. Optical and Structural Properties of Al₂O₃ Doped ZnO Nanotubes
1717 Prepared by Ald and Their Photocatalytic Application. *Surf. Coat.*
1718 *Technol.* **2018**, *343*, 24–29.
- 1719 (122) Dai, H.-Q.; Xu, H.; Zhou, Y.-N.; Lu, F.; Fu, Z.-W.
1720 Electrochemical Characteristics of Al₂O₃-Doped ZnO Films by
1721 Magnetron Sputtering. *J. Phys. Chem. C* **2012**, *116*, 1519–1525.
- 1722 (123) Santala, E.; Kemell, M.; Leskela, M.; Ritala, M. The
1723 Preparation of Reusable Magnetic and Photocatalytic Composite
1724 Nanofibers by Electrospinning and Atomic Layer Deposition.
1725 *Nanotechnology* **2009**, *20*, 035602.
- 1726 (124) Celebioglu, A.; Ranjith, K. S.; Eren, H.; Biyikli, N.; Uyar, T.
1727 Surface Decoration of Pt Nanoparticles Via Ald with Tio₂ Protective
1728 Layer on Polymeric Nanofibers as Flexible and Reusable Heteroge-
1729 neous Nanocatalysts. *Sci. Rep.* **2017**, *7*, 13401.
- 1730 (125) Topuz, F.; Uyar, T. Atomic Layer Deposition of Palladium
1731 Nanoparticles on a Functional Electrospun Poly-Cyclodextrin Nano-
1732 web as a Flexible and Reusable Heterogeneous Nanocatalyst for the
1733 Reduction of Nitroaromatic Compounds. *Nanoscale Adv.* **2019**, *1*,
1734 4082–4089.
- 1735 (126) Dwyer, D. B.; Lee, D. T.; Boyer, S.; Bernier, W. E.; Parsons, G.
1736 N.; Jones, W. E. Toxic Organophosphate Hydrolysis Using Nanofiber-
1737 Templated UiO-66-Nh₂Metal–Organic Framework Polycrystalline
1738 Cylinders. *ACS Appl. Mater. Interfaces* **2018**, *10*, 25794–25803.
- 1739 (127) Arslan, O.; Eren, H.; Biyikli, N.; Uyar, T. Reusable and
1740 Flexible Heterogeneous Catalyst for Reduction of Tnt by Pd
1741 Nanocube Decorated ZnO Nanolayers onto Electrospun Polymeric
1742 Nanofibers. *ChemistrySelect* **2017**, *2*, 8790–8798.
- 1743 (128) Veluru, J. B.; Manippady, K. K.; Rajendram, M.; Mya Mya, K.;
1744 Rayavarapu, P. R.; Appukkuttan, S. N.; Seeram, R. Photocatalytic
1745 Hydrogen Generation by Splitting of Water from Electrospun Hybrid
1746 Nanostructures. *Int. J. Hydrogen Energy* **2013**, *38*, 4324–4333.
- 1747 (129) Babu, V. J.; Kumar, M. K.; Nair, A. S.; Kheng, T. L.;
1748 Allakhverdiev, S. I.; Ramakrishna, S. Visible Light Photocatalytic
1749 Water Splitting for Hydrogen Production from N-Tio₂ Rice Grain
1750 Shaped Electrospun Nanostructures. *Int. J. Hydrogen Energy* **2012**, *37*,
1751 8897–8904.
- 1752 (130) Du, Q.; Wu, J.; Yang, H. Pt@Nb-Tio₂ Catalyst Membranes
1753 Fabricated by Electrospinning and Atomic Layer Deposition. *ACS*
1754 *Catal.* **2014**, *4*, 144–151.
- 1755 (131) Khalily, M. A.; Patil, B.; Yilmaz, E.; Uyar, T. Atomic Layer
1756 Deposition of Co₃O₄ Nanocrystals on N-Doped Electrospun Carbon

- 1757 Nanofibers for Oxygen Reduction and Oxygen Evolution Reactions.
1758 *Nanoscale Advances* **2019**, *1*, 1224–1231.
- 1759 (132) Barhoum, A.; El-Maghrabi, H. H.; Iatsunskyi, I.; Coy, E.;
1760 Renard, A.; Salameh, C.; Weber, M.; Sayegh, S.; Nada, A. A.;
1761 Roualdes, S.; Bechelany, M. Atomic Layer Deposition of Pd
1762 Nanoparticles on Self-Supported Carbon-Ni/Nio-Pd Nanofiber
1763 Electrodes for Electrochemical Hydrogen and Oxygen Evolution
1764 Reactions. *J. Colloid Interface Sci.* **2020**, *569*, 286–297.
- 1765 (133) Schlicht, S.; Assaud, L.; Hansen, M.; Lickleder, M.;
1766 Bechelany, M.; Perner, M.; Bachmann, J. An Electrochemically
1767 Functional Layer of Hydrogenase Extract on an Electrode of Large
1768 and Tunable Specific Surface Area. *J. Mater. Chem. A* **2016**, *4*, 6487–
1769 6494.
- 1770 (134) Du, Q.; Wu, J.; Yang, H. Pt@Nb-Tio2 Catalyst Membranes
1771 Fabricated by Electrospinning and Atomic Layer Deposition. *ACS*
1772 *Catal.* **2014**, *4*, 144–151.
- 1773 (135) Li, Y.; Sun, Y.; Xu, G.; Lu, Y.; Zhang, S.; Xue, L.; Jur, J. S.;
1774 Zhang, X. Tuning Electrochemical Performance of Si-Based Anodes
1775 for Lithium-Ion Batteries by Employing Atomic Layer Deposition
1776 Alumina Coating. *J. Mater. Chem. A* **2014**, *2*, 11417–11425.
- 1777 (136) Wee, G.; Soh, H. Z.; Cheah, Y. L.; Mhaisalkar, S. G.;
1778 Srinivasan, M. Synthesis and Electrochemical Properties of Electro-
1779 spun V2o5 Nanofibers as Supercapacitor Electrodes. *J. Mater. Chem.*
1780 **2010**, *20*, 6720–6725.
- 1781 (137) Kim, B.-H.; Kim, C. H.; Yang, K. S.; Rahy, A.; Yang, D. J.
1782 Electrospun Vanadium Pentoxide/Carbon Nanofiber Composites for
1783 Supercapacitor Electrodes. *Electrochim. Acta* **2012**, *83*, 335–340.
- 1784 (138) Cho, S.; Kim, D.-H.; Lee, B.-S.; Jung, J.; Yu, W.-R.; Hong, S.-
1785 H.; Lee, S. Ethanol Sensors Based on ZnO Nanotubes with
1786 Controllable Wall Thickness Via Atomic Layer Deposition, an O2
1787 Plasma Process and an Annealing Process. *Sens. Actuators, B* **2012**,
1788 *162*, 300–306.
- 1789 (139) Katoch, A.; Abideen, Z. U.; Kim, J.-H.; Kim, S. S. Influence of
1790 Hollowness Variation on the Gas-Sensing Properties of ZnO Hollow
1791 Nanofibers. *Sens. Actuators, B* **2016**, *232*, 698–704.
- 1792 (140) Choi, S.-W.; Park, J. Y.; Kim, S. S. Synthesis of Sno2-Zno
1793 Core-Shell Nanofibers Via a Novel Two-Step Process and Their Gas
1794 Sensing Properties. *Nanotechnology* **2009**, *20*, 465603.
- 1795 (141) Park, J. Y.; Choi, S.-W.; Kim, S. S. A Model for the
1796 Enhancement of Gas Sensing Properties in Sno2-Zno Core-Shell
1797 Nanofibers. *J. Phys. D: Appl. Phys.* **2011**, *44*, 205403.
- 1798 (142) Katoch, A.; Choi, S.-W.; Sun, G.-J.; Kim, S. S. An Approach to
1799 Detecting a Reducing Gas by Radial Modulation of Electron-Depleted
1800 Shells in Core-Shell Nanofibers. *J. Mater. Chem. A* **2013**, *1*, 13588–
1801 13596.
- 1802 (143) Viter, R.; Chaaya, A. A.; Iatsunskyi, I.; Nowaczyk, G.;
1803 Kovalevskis, K.; Erts, D.; Miele, P.; Smyntyna, V.; Bechelany, M.
1804 Tuning of ZnO 1d Nanostructures by Atomic Layer Deposition and
1805 Electrospinning for Optical Gas Sensor Applications. *Nanotechnology*
1806 **2015**, *26*, 105501.
- 1807 (144) Chaaya, A. A.; Bechelany, M.; Balme, S.; Miele, P. ZnO 1d
1808 Nanostructures Designed by Combining Atomic Layer Deposition
1809 and Electrospinning for Uv Sensor Applications. *J. Mater. Chem. A*
1810 **2014**, *2*, 20650–20658.
- 1811 (145) Vempati, S.; Ozcan, S.; Uyar, T. Temporary and Permanent
1812 Changes to the Defect Equilibrium Due to Ultraviolet Exposure:
1813 Surface and Bulk Effects on ZnO Nanostructures. *Appl. Surf. Sci.* **2018**,
1814 *457*, 676–683.
- 1815 (146) Vempati, S.; Ozcan, S.; Uyar, T. Temporary and Permanent
1816 Changes to the Defect Equilibrium Due to Ultraviolet Exposure:
1817 Surface and Bulk Effects on ZnO Nanostructures. *Appl. Surf. Sci.*
1818 **2018**, *457*, 676–683.